Sensible heat thermal energy storage performance of mono and blended nanofluids in a free convective-radiation inclined system

Oguzhan Kazaz [a], Rosalia Ferraro [b], Manlio Tassieri [c], Shanmugam Kumar [a], Gioia Falcone [a], Nader Karimi [a,d], Manosh C. Paul [a,*]

[a] Systems, Power & Energy Research Division, James Watt School of Engineering, University of Glasgow, Glasgow, G12 8QQ, UK
[b] Department of Chemical, Materials and Industrial Production Engineering (DICMAPI), University of Naples Federico II, P.le Tecchio 80, 80125, Naples, Italy
[c] Division of Biomedical Engineering, James Watt School of Engineering, University of Glasgow, Glasgow, G12 8LT, UK
[d] School of Engineering and Materials Science, Queen Mary University of London, London, E1 4NS, UK

HIGHLIGHTS

- Photothermal performance of a nanoparticle based solar collector is experimentally and numerically investigated.
- Attenuation of pure working fluid is augmented by nanoparticles.
- Improving nanoparticle diameter enhances temperature gain.
- Blended nanoparticles further enhance useful heat capacity.
- Tilt angle diminishes thermal capacity of the collector.

ARTICLE INFO

ABSTRACT

The photothermal conversion performance (PCP) of a nanofluid-based solar energy system is investigated numerically and experimentally. The impacts of particle size, volume concentration, nanoparticle type, base fluid type and collector inclination angle on the PCP are investigated. It is observed that using nanoparticles improves the ability to absorb solar energy. Temperature gain is 2.2, 3.2, 3.8, 4.2, and 9 times better than pure water for water-based Al, Al_2O_3, Au, Cu, and Graphite mono nanofluids, respectively. Interestingly, blended nanofluids containing the same nanoparticles significantly argument the optical properties, with useful heat enhancement ranging from 62.8 (mono) to 194 kJ/kg (hybrid). However, the collector's inclination angle, which ranges from 0 to 60°, has a negative impact on the PCP by reducing the solar radiation absorption of the nanofluids due to a decrease in the radiation penetrating the collector. Furthermore, as nanoparticle size increases, so does the thermal performance of the nanofluid. An experimental investigation is carried out for pure water and nanofluid at various wind speeds and solar irradiation levels ranging from 1 to 4 m/s and 200–1000 W/m^2, respectively, to validate the numerical results.

Nomenclature

H	Collector height (m)

$\vec{r}$	Position vector
$Q_{a\lambda}$	Absorption efficiency
L	Collector length (m)
α	Size parameter
h	Convective heat transfer coefficient (W/m^{2}K)
p	Pressure (Pa)
$\vec{s}'$	Scattering direction vector
$K_{s\lambda}$	Scattering coefficient (1/m)
D	Particle diameter (m)
FVM	Finite volume method
$Q_{e\lambda}$	Extinction efficiency
ΔT	Temperature change (K)
I_λ	Radiation intensity (W/m^{2}μm)
$K_{e\lambda}$	Extinction coefficient (1/m)
k	Thermal conductivity (W/mK)
$Q_{s\lambda}$	Scattering efficiency
n	Refractive index
AR	Aspect ratio
f_v	Particle volume fraction
g	Gravitational acceleration (m/s^2)
k	Absorption index
u, v	Velocity vectors (m/s)
w	Wind speed (m/s)
L/H	Aspect ratio
T_0	Initial temperature (K)
$K_{a\lambda}$	Absorption coefficient (1/m)
T	Temperature (K)
$\vec{s}$	Direction vector
C_p	Specific heat (J/kgK)
q	Heat flux (W/m^2)
$I_{b\lambda}$	Black body intensity (W/m^{2}μm)
PCP	Photothermal conversion performance
m	Normalized refractive index of the particle to the fluid

Greek symbols

φ	Collector inclination angle (∘)
ρ	Density (kg/m^3)
λ	Wavelength of incident light (μm)
β	Thermal expansion coefficient (1/K)
Φ	Phase function
μ	Dynamic viscosity (Ns/m^2)
ε	Emissivity
Ω'	Solid angle
σ	Stefan-Boltzmann constant (5.67×10^{-8} W /m^{2}K^4)

Subscripts

r	Radiative
nf	Nanofluid
amb	Ambient

1. Introduction

The ubiquity of solar energy provides an important opportunity for the development of sustainable energy to maintain the balance between energy supply and demand. Solar heating systems enable an easy use of solar energy in a low temperature based solar energy application at domestic/residential applications [1]. However, in order to realise this potential advantage, it is first necessary to use a solar collector in buildings for capturing and converting the sun's rays into thermal energy [2]. In a widely used conventional flat plate solar collector, solar irradiation is absorbed and transferred to heat exchanger pipes, and then this energy is transferred to fluid. In this way, heat transfer takes place indirectly, and energy absorbed and transferred is affected by heat loss which negatively impacts the solar collector's performance. However, in a direct absorption solar collector (DASC) or a volumetrically heated solar collector, where

heat transfer fluid is utilized as an absorbing medium, solar irradiation is directly absorbed by the working fluid and converted into thermal energy, thereby enhancing the performance of collector [3,4].

However, the most significant factor impacting the system capacity in a solar energy collector is the heat transfer fluid. Especially, in a system when the working fluid is directly or volumetrically heated by solar energy, the radiative characteristics of working fluid become important. A standard/pure working fluid such as water has an insufficient solar energy absorption capacity due to its low optical properties, therefore efficiency of the system could be low. One of the ways to augment the system's efficiency is by using nanofluids [5–8]. Applications of nanofluids, that are formed by dispersing nanoparticles homogeneously in a base fluid such as water, in solar energy applications are increasing [5,9–11]. Due to the high optical and thermophysical characteristics of nanoparticles, they have the potential to improve the system performance by increasing the solar energy capture and by also improving both the thermophysical and radiative behaviours [12–14]. Lin et al. [15] experimentally explored the optical properties of glycol-based Ag nanofluids at high temperatures. Beer-Lambert model which includes the temperature effect was developed and according to their results, Ag/glycol nanofluid had superior optical properties with a localised surface plasmon resonance at a wavelength of 445 nm. It was further reported that the absorption index of nanofluid decreased as temperature augmented, but the peak shape of the absorption index narrowed. The temperature dependent optical properties of nanofluid were also well achieved by the developed model.

Sani et al. [16] reported the optical properties of graphite/nanodiamond nanoparticles dispersed in ethylene glycol. They prepared different ash contents such as 5.9% and 0.3%wt in powder with different concentrations as 0.0025%, 0.005%, 0.01% wt in the fluid they used. A high sunbeam extinction was found with a full absorption at 15 mm and 30 mm path lengths for 0.01% and 0.005% wt, respectively. This study also suggested that this nanofluid type, which shows a lower transmittance than a pure base liquid, could be used in DASC applications due to its high sunlight absorption. Guo et al. [17] experimentally carried out the optical and photothermal conversion characteristics of lanthanum hexaboride (LaB_6) nanoparticles dispersed in water. They noticed that LaB_6 nanoparticles had cubic crystal phase crystal structures and found that when water based LaB_6 nanofluid with a mass concentration of 200 ppm was exposed to sunbeam for 3500 s, its temperature increased up to 58 °C. In addition, PCP of LaB_6/water nanofluid was augmented as the mass fraction augmented and particularly, the mass fractions of 100 and 200 ppm showed having over 90% solar photothermal conversion efficiency below 40 °C. Within the similar context, Kumar et al. [18] explored both the thermal performance and optical properties of carbon-solar glycol nanofluids at different volume concentrations of 2000, 4000, and 6000 ppm. They synthesized the leaves of Kigelia africana into porous activated carbon nanomaterials. The experimental study unveiled that the nanofluid's thermal conductivity was improved by 14.36% with the addition of carbon at a volume concentration of 6000 ppm. It was further revealed that the nanofluid's utmost temperature difference compared to solar glycol as the host fluid was 10 °C at the same volume concentration. Furthermore, the efficiency of the activated carbon-based nanofluid was found to be up to 94.51% during 600 s of sunlight.

Huaxu et al. [19] examined the radiative heat transfer and optical behaviours of ZnO nanoparticles using a combination of Mie scattering and Monte Carlo ray tracing techniques. They also analysed the impacts of mass fraction, optical length, and particle diameter of glycol/ZnO nanofluid. Their results revealed that the spectral transmittance of glycol/ZnO nanofluid enhanced with optical length but decreased with both particle concentration and size. It was further discovered that the entire efficient spectral transmittance co-efficient using water/ZnO nanofluid was 21.54%, which was better than water/polypyrrole nanofluid. Hatami and Jing [20] compared the thermal performances of wavy and flat DASCs using dissimilar nanofluids: TiO_2/water, Al_2O_3/water, and CuO/water. Their numerical findings betrayed that the wavy bottom-wall collector had a greater local Nusselt number whereas the flat plate-wall collector had a better mean Nusselt number. It was also found that the TiO_2/water nanofluid improves the mean Nusselt number compared to the other nanofluids. Beicker et al. [21] analysed the photothermal conversion characteristics of water based gold and multi-walled carbon nanotubes at a volume concentration 1–40 ppm and 1–300 ppm, respectively. The results disclosed that nanofluid with a low particle concentration provides higher thermal performance, e.g. the optimal particle concentration for gold and multi-walled carbon nanotubes nanofluids was found to be 20 and 10 ppm, respectively, to attain best performance.

Turkyilmazoglu [22] studied the heat transfer characteristics of a tilted DASC employing Al_2O_3/water. An analytical model was established to evaluate the influence of applied boundary conditions that are isothermal and non-adiabatic to the base panel. The outlet fluid temperature was augmented with these boundary conditions compared to an adiabatic case. Hatami et al. [23] also analysed an inclined DASC using hybrid finite difference and differential transformation methods. Two various boundary conditions, convection heat transfer, and constant temperature were examined for the base of the collector, and it was revealed that increasing the cavity base temperature boosted the fluid's temperature. The outcomes further displayed that as the volume concentration of Al_2O_3 enhanced, the collector's thermal capacity improved. Cregan and Myers [24] analytically explored an inclined Al/water nanofluid based DASC collector in the low-mid temperature range coupling radiative transport. The method of separation of variables was used to further examine the collector's efficiency. Their findings discovered that the collector efficiency and nanofluid outlet's mean temperature improved as the nanoparticle fraction, nanoparticle size and collector height enhanced.

For the utilization of a building integrated solar thermal collector, it is required to be installed on the facades or roofs of a building. Although solar collectors can be adjusted with a fixed installation angle, a change in the orientational angle can affect not only a single collector but also the overall system capacity. It is unknown how different inclination angles affect the energy storage capacity of a solar collector when the PCP of a working fluid containing either mono or hybrid nanoparticles is taken into account. It is intriguing to scrutinize the heat transfer behaviours of blended nanofluids in a translucent medium, since previous papers do not consider the hybrid nanoparticles. Moreover, the performance of a nanofluid is affected by volume concentration, particle size and Brownian motion; however, it is currently unknown how these factors influence the photothermal conversion of a semi-transparent medium based tilted nanofluid storage system. In addition, as per the literature, different types of working fluid, such as glycol, can be used. However, a comparative analysis of water, Therminal VP1 and ethylene glycol principal fluids is lacking. This paper aims to fill these research gaps by numerically investigating combined radiative heat transfer and free convection of nanofluids at different inclination angles of a
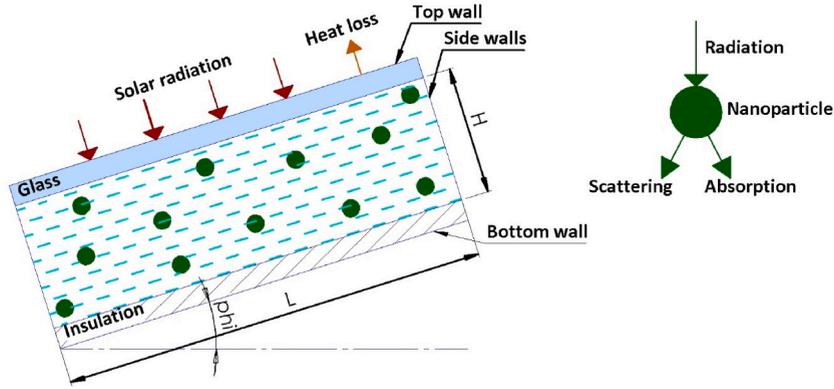
Fig. 1. The schematic of a two-dimensional nanofluid based inclined solar energy system.

solar collector. This is also the first study in which the impacts of internal irradiation are observed in volumetrically heated nanofluids in a convective tilted system. Further, experiments are carried out to validate the model and further investigate the characteristics of nanofluid thermal storage.

2. Problem statement and mathematical formulation

A two-dimensional model of an inclined solar energy storage system having the *L/H* of 10 [12] is developed, as illustrated in Fig. 1. Sun's rays penetrating through the nanoparticles of host fluid are absorbed due to the scattering and absorption characteristics of the nanoparticles. The top plate is exposed to the ambient, hence it is assumed to lose heat by combined convection and radiation. In addition, the base and side panels are regarded as adiabatic since it is used for heat storage.

The Radiative Transport Equation is implemented to explain the irradiation's spectral attenuation inside the semi-transparent flow medium as [25]:

$$\nabla \bullet (I_\lambda(\overrightarrow{r}, \overrightarrow{s})\overrightarrow{s}) + (K_{a\lambda} + K_{s\lambda})I_\lambda(\overrightarrow{r}, \overrightarrow{s}) = K_{a\lambda}n^2 I_{b\lambda} + \frac{K_{s\lambda}}{4\pi}\int_0^{4\pi} I_\lambda(\overrightarrow{r}, \overrightarrow{s'})\Phi(\overrightarrow{s} \bullet \overrightarrow{s'})d\Omega' \tag{1}$$

Scattering effects can be neglected in pure fluids due to the domination of absorption into attenuation. Hence, the extinction coefficient can be identified as [26]:

$$K_{e\lambda,f} = K_{a\lambda,f} = \frac{4\pi k}{\lambda} \tag{2}$$

Components such as nanoparticle volume concentration or nanoparticle size, on the other hand, can impact the absorption and scattering behaviours of nanofluids and change the radiation effects of a translucent medium. Therefore, Rayleigh scattering contributes to the calculation of the optical characteristics of nanoparticles [27], and hence, the extinction coefficient can be re-described as [26]:

$$K_{e\lambda,p} = \frac{3f_v Q_{e\lambda}(\alpha, m)}{D} \tag{3}$$

where *m* and *α* can be identified as [26]:

$$m = \frac{m_{particles}}{n_{fluid}} \tag{4}$$

$$m_{particles} = n + ik \tag{5}$$

$$\alpha = \frac{\pi D}{\lambda} \tag{6}$$

The optical properties can also be found in the literature [28–32], and the extinction efficiency is defined as [27]:

$$Q_{e\lambda} = Q_{a\lambda} + Q_{s\lambda} \tag{7}$$

where

$$Q_{s\lambda} = \frac{8}{3}\alpha^4 \left| \left(\frac{m^2 - 1}{m^2 + 2}\right) \right|^2 \tag{8}$$

Table 1

Thermophysical properties of nanoparticles [36–39].

Properties	Al	Graphite	Au	Al_2O_3	Cu
C_p (J/kgK)	900	709	128.8	765	383
k (W/mK)	247	1950	314.4	40	400
ρ (kg/m^3)	2700	2210	19320	3970	8954

$$Q_{a\lambda} = 4\alpha Im \left\{ \frac{m^2-1}{m^2+2} \left[1 + \frac{\alpha^2}{15} \left(\frac{m^2-1}{m^2+2} \right) \frac{m^4 + 27m^2 + 38}{2m^2+3} \right] \right\} \tag{9}$$

The nanofluid's effective extinction coefficient is the total of the extinction coefficient of a base fluid and nanoparticles:

$$K_{e\lambda,nf} = K_{e\lambda,p} + K_{e\lambda,f} \tag{10}$$

Moreover, the extinction coefficient of a blended nanofluid is the sum of the extinction coefficients of host fluid and each nanoparticle [13]:

$$K_{e\lambda,hybrid\ nf} = K_{e\lambda,f} + K_{e\lambda,p1} + K_{e\lambda,p2} \tag{11}$$

The fluid flow within the collector is presumed to be laminar, incompressible, Newtonian, and steady state. The continuity, momentum and energy equations are, respectively, given as:

$$\frac{\partial u}{\partial x} + \frac{\partial v}{\partial y} = 0 \tag{12}$$

$$\rho_{nf} \left(u \frac{\partial u}{\partial x} + v \frac{\partial u}{\partial y} \right) = -\frac{\partial p}{\partial x} + \mu_{nf} \left(\frac{\partial^2 u}{\partial x^2} + \frac{\partial^2 u}{\partial y^2} \right) + g \sin \varphi (\rho\beta)_{nf} (T - T_o) \tag{13}$$

$$\rho_{nf} \left(u \frac{\partial v}{\partial x} + v \frac{\partial v}{\partial y} \right) = -\frac{\partial p}{\partial x} + \mu_{nf} \left(\frac{\partial^2 v}{\partial x^2} + \frac{\partial^2 v}{\partial y^2} \right) + g \cos \varphi (\rho\beta)_{nf} (T - T_o) \tag{14}$$

$$\rho_{nf} C_{P_{nf}} \left(u \frac{\partial T}{\partial x} + v \frac{\partial T}{\partial y} \right) = k_{nf} \left(\frac{\partial^2 T}{\partial x^2} + \frac{\partial^2 T}{\partial y^2} \right) - \nabla \bullet q_r \tag{15}$$

The energy conservation is coupled with the Radiative Transport Equation. Thus, the radiative heat flux's divergence is determined as [33]:

$$\nabla \bullet q_r = K_{a\lambda} \left[4\pi I_{b\lambda} - \int_0^{4\pi} I_\lambda (\overrightarrow{r}, \overrightarrow{s}') d\Omega' \right] \tag{16}$$

Subsequently, the boundary conditions are:

at the side plates:

$$\frac{\partial T}{\partial x} = 0 \tag{17}$$

at all the solid boundaries:

$$u = v = 0 \tag{18}$$

at the base plate:

$$\frac{\partial T}{\partial y} = 0 \tag{19}$$

at the top plate:

$$q = h(T - T_{amb}) + \varepsilon\sigma \left(T^4 - T_{amb}^4 \right) \tag{20}$$

where h is defined as [34]:

$$h = 5.7 + 3.8w \tag{21}$$

In the previous research of Kazaz et al. [35], a comprehensive information is available on how to determine the thermophysical properties of nanofluids. The nanofluids' thermophysical properties are presumed to be constant apart from the density, that is derived by the Boussinesq approximation. The thermophysical characteristics of the various nanoparticles are also shown in Table 1.
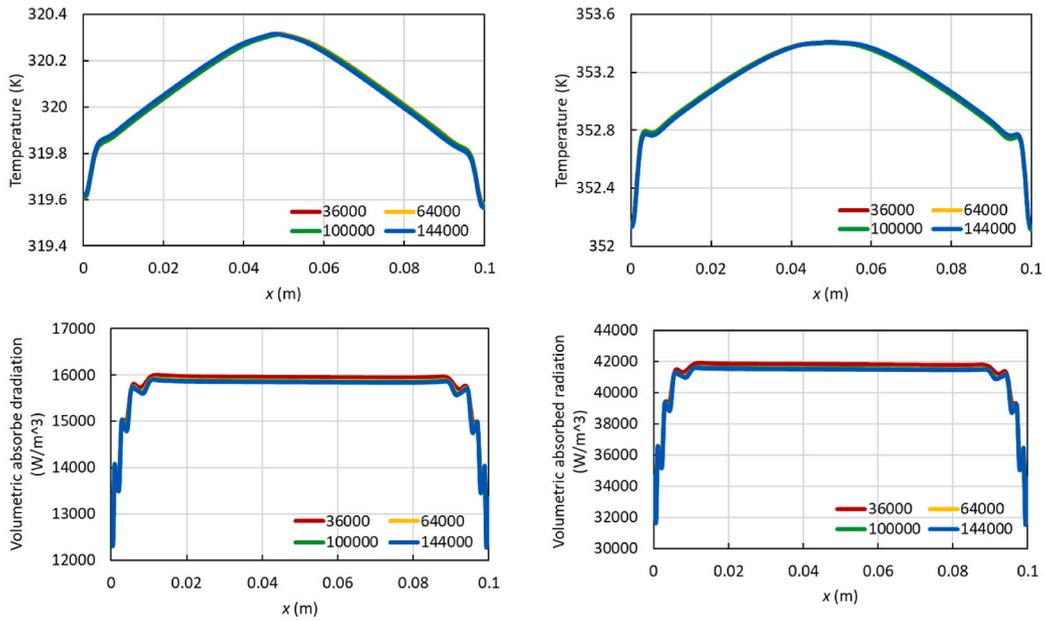
Fig. 2. Effect of different mesh numbers along the horizontal midline at the inclination angle of 0 (zero) degree (left frames: Al/water nanofluid, right frames: Al + Al$_2$O$_3$/water nanofluid).

Table 2
Effect of different grid sizes with varying inclination angle.

Nanofluid type	Inclination angle (∘)	Grid size	Mean fluid temperature (K)	Mean volumetric absorbed radiation (kW/m^3)
Al/water	0	36000	319.955	29.701
		64000	319.954	29.700
		100000	319.954	29.700
		144000	319.953	29.700
	30	36000	317.713	25.605
		64000	317.712	25.604
		100000	317.711	25.603
		144000	317.711	25.603
	60	36000	311.978	14.783
		64000	311.978	14.782
		100000	311.977	14.782
		144000	311.977	14.781
Al + Al$_2$O$_3$/water	0	36000	352.816	92.361
		64000	352.814	92.361
		100000	352.813	92.360
		144000	352.813	92.360
	30	36000	345.757	79.516
		64000	345.754	79.511
		100000	345.753	79.509
		144000	345.752	79.506
	60	36000	328.199	45.671
		64000	328.191	45.653
		100000	328.190	45.652
		144000	328.190	45.651

Finally, the useful heat gains in the solar system can be defined as [40]:

$$q_{useful\ heat} = C_p\ \Delta T \tag{22}$$

2.1. Numerical procedure and grid independence test

ANSYS Fluent 2020 R1 is used to solve the energy and Navier-Stokes equations by applying a pressure-based FVM. The Discrete Ordinates approach is chosen for the Radiative Transport Equation which includes the impacts of emitting, absorption, and scattering components. The DO method is the directional deviation of the irradiation power. Therefore, the transfer equation is resolved by spanning the 4π entire solid angles [41]. The second-order differencing scheme is utilized for discretisation of equations, and the velocity-pressure coupling is presented by the SIMPLE algorithm. Least Square Cell Based is adjusted for diffusion terms and velocity
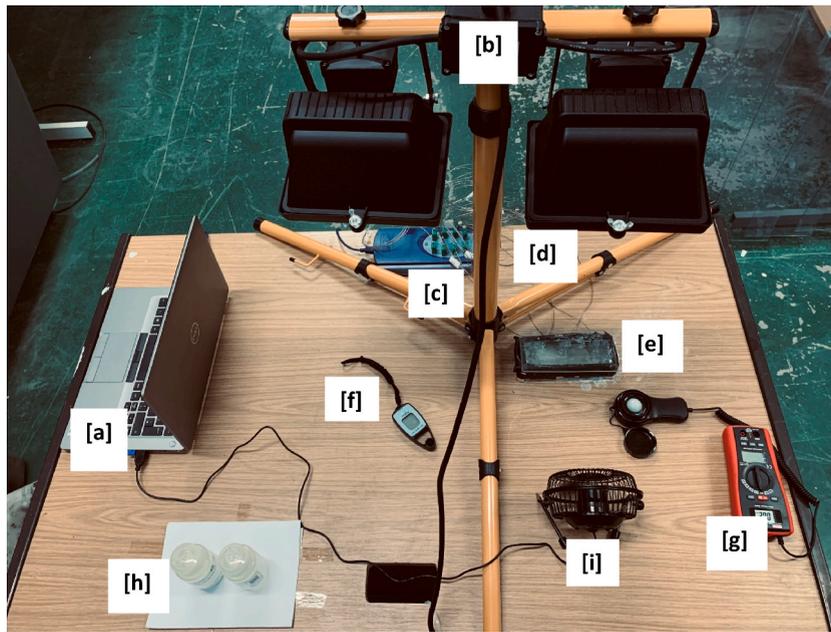
Fig. 3. Image of the experimental setup (a) laptop, (b) light source, (c) data logger, (d) thermocouples, (e) storage cavity, (f) anemometer, (g) solar power meter, (h) heat transfer fluid, and (i) fan.
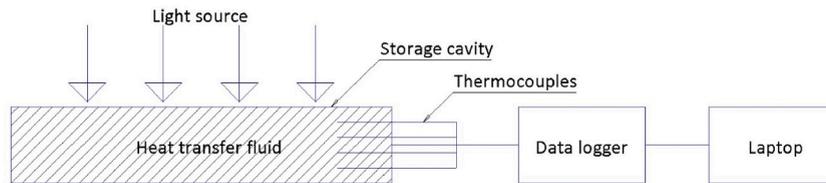

Fig. 4. Schematic layout of the experimental system.

derivatives. PRESTO! is also chosen for the discretisation of the momentum equations. The residual levels of the DO and energy equations are kept under 10^{-6} whereas for the other governing equations are under 10^{-5}. 3×3 pixelization and 5×5 divisions are employed in order to get more rational results [25]. Furthermore, the comprehensive information about the numerical procedure is found in the earlier works of the authors [9,35].

A sensitivity analysis is performed so that the numerical results do not change on the grid numbers. For that, four different grid analyses taking as 36000, 64000, 100000 and 144000 are carried out for Al/water and Al + Al_2O_3/water nanofluids at a volume concentration of 75 ppm. Fig. 2 displays the collector performance in terms of the volumetric absorbed radiation and temperature along the horizontal midline of the storage cavity with various grid numbers for a fixed inclination angle. Table 2 show further details about the behaviour of these mesh numbers at the different inclination angles. The mesh numbers of 64000 can be selected for further numerical simulations due to more uniformity in the overall results and also considering the computational time it took to complete each model.

3. Experimental procedures

The PCP of water based Al_2O_3 nanofluid with a high-volume concentration is experimentally investigated in order to first provide data for numerical model validation. The closed storage cavity made of aluminium, whose schematic diagram was given in Fig. 1, is designed and the experimental system is set up as illustrated in Figs. 3 and 4. The experimental system consists of a PC, light source, data logger, thermocouple (K type), storage cavity, anemometer, solar power meter, heat transfer fluid and small fan. The storage cavity whose volume is 225 cm^3 with the width of 5 cm was initially filled with pure water, and then Al_2O_3/water nanofluid (mass concentration of 0.22) is used as a working fluid. Al_2O_3/water nanofluid was provided by Nanografi Nano Technology, and an electron microscopy was utilized to understand the morphology of Al_2O_3 nanoparticles dispersed in water. As also shown in Fig. 5, nano-particles are well dispersed in water as a host fluid. A solar simulator using a 500 W halogen lamp, which is similar to the one used in other studies such as [42,43], was applied to heat the working fluid. The heat flux value reaching the glass surface was measured by the solar power meter, and the required heat flux was obtained by moving the sun simulator vertically. The thermocouples were also placed inside the cavity in order to measure the temperature change in the storage cavity and transmitted to the computer via a data
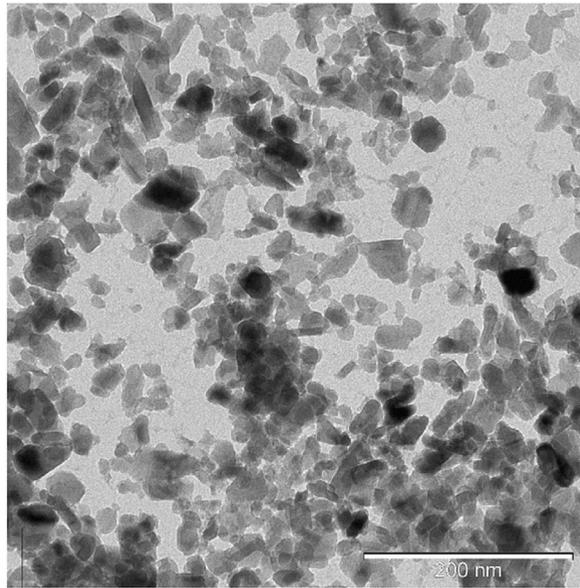
Fig. 5. Electron microscopy image of Al_2O_3 nanoparticles dispersed in water.
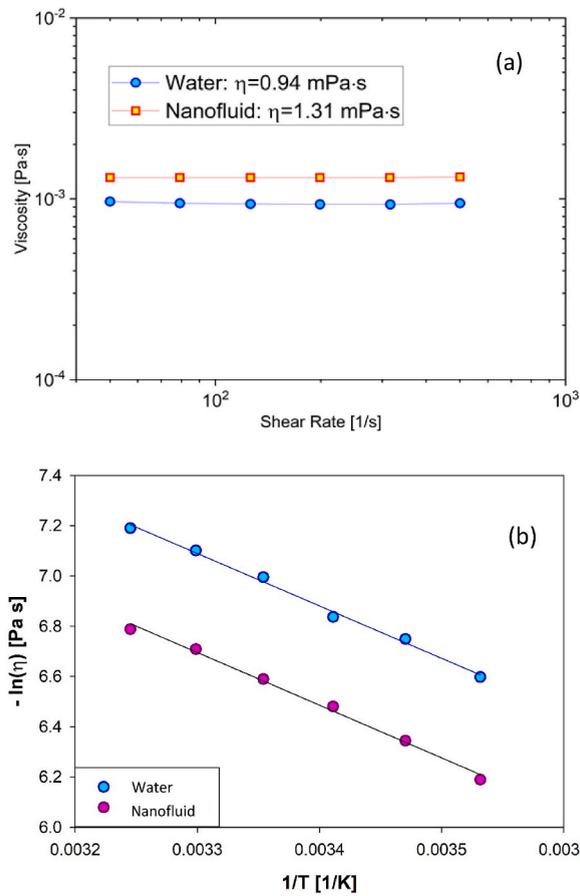

Fig. 6. (a) The viscosity measurements of Al_2O_3/water nanofluid and water at a reference temperature of 25 °C. (b) The negative natural logarithm of viscosity, -ln(η), versus of the inverse of temperature, 1/T, for Al_2O_3/water nanofluid (pink circles) and pure water (blue circles). For both systems, E_a was estimated from the slope of linear curve (solid line), obtained by fitting experimental data by means of an Arrhenius law.
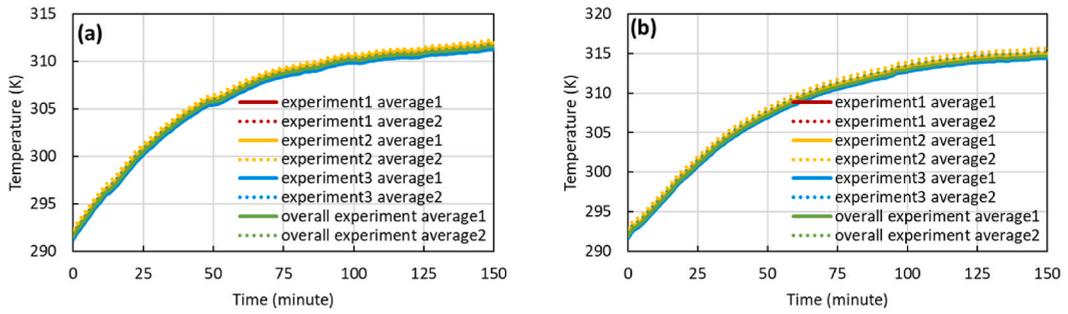
Fig. 7. Stability analysis of the experimental setup (a) water, and (b) Al$_2$O$_3$/water nanofluid.
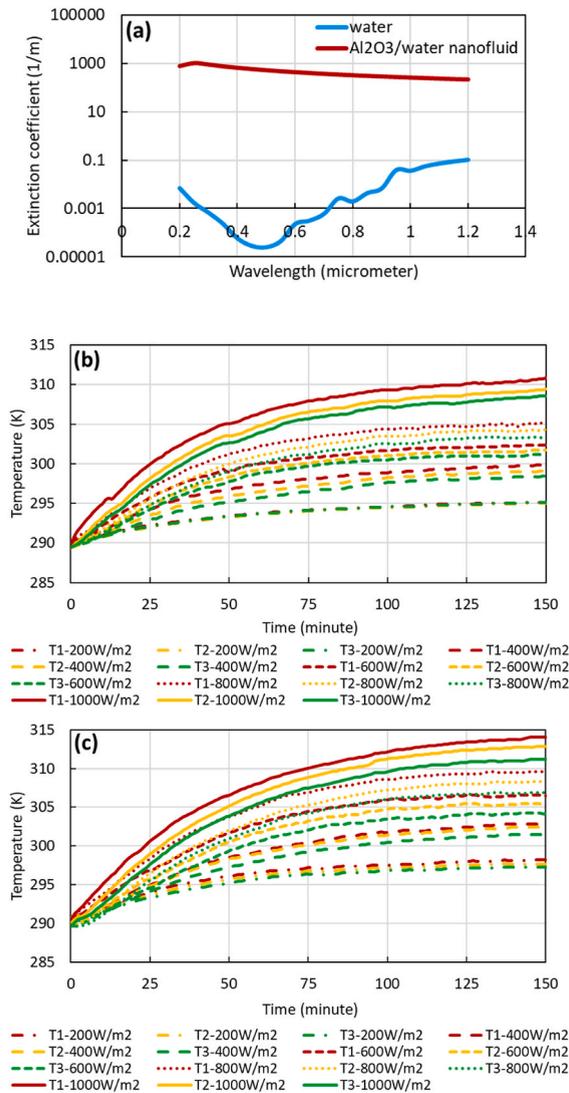

Fig. 8. (a) Extinction coefficients of water and Al$_2$O$_3$/water nanofluid in logarithmic scale (m^{-1}), experimental results of temperature distribution of (b) water, and (c) Al$_2$O$_3$/water nanofluid inside the cavity under various irradiances/heat fluxes.
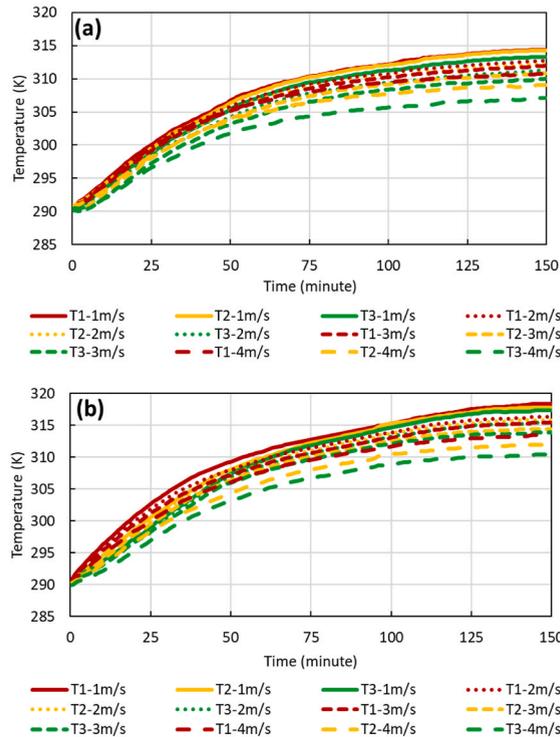
Fig. 9. Experimental results of temperature distribution of (a) water, and (b) Al$_2$O$_3$/water nanofluid inside the cavity under various wind speeds.

logger. Finally, wind speed was measured with an anemometer, to determine the convective heat transfer coefficient on the top facet of the cavity.

Depending on the viscosity of the fluid, the heat transfer by free convection may be affected in the cavity. For this reason, rheological measurements were performed at different temperatures (i.e., from 10 °C to 35 °C, in increments of 5 °C) using a stress-controlled rheometer (Anton Paar Physica MCR 302 Instruments) equipped with a cone-plate measuring system (CP60-1-SN42255). The temperature was controlled by means of a Peltier system connected to a water bath. The fluid viscosity (η) was measured by performing a flow curve test at shear rates varying within the range of 50–500 1/s. For each of the explored temperatures, the fluid viscosity had a constant value within the range of measured shear rates. Fig. 6(a) shows the measured viscosity of Al$_2$O$_3$/water nanofluid and water at a reference temperature of 25 °C against the shear rates with a Newtonian relationship. Moreover, in order to get the activation energy (E_a) of the Al$_2$O$_3$/water nanofluid, in Fig. 6(b) the negative natural logarithm of the viscosity values, -ln(η), are drawn versus the inverse of temperature, 1/T, (pink circles) and compared with those measured for pure water (blue circles). For both the fluids, E_a was evaluated by performing a linear fit (solid line) of the data, and by assuming that those adhere to the Arrhenius law. As shown in Fig. 6(b), η of Al$_2$O$_3$/water nanofluid decreases with increasing temperature with a slope similar to that of pure water (i.e., 17.45 kJ/mol and 17.34 kJ/mol, respectively). Finally, the results of the viscosity measurement are applied for the numerical model's validation.

4. Results and discussion

This part is divided into two main sub-sections, starting with the experimental results and model validation followed by the investigation of the numerical results.

4.1. Experimental results and numerical validation

In order to ensure the stability of the experimental results, experiment of the storage cavity filled with water was repeated three times under the same conditions, and the mean temperatures of the water were examined. For this, two different average temperature values were used: the first average temperature was obtained by using three different thermocouples, while six different thermocouples were used for the second average temperature. The same results were obtained from the three different experiments as indicated in Fig. 7, and it also turned out to be the same when the two different average temperatures are compared. This indicates that the current experimental setup is reliable, and it is also uncovered that the working fluid reaches the steady state condition from the 125th minutes. In addition, all the other walls of the cavity, except the upper wall, were covered with insulation materials to suspend thermal losses. Further, since the experiment was carried out in a laboratory, that is, in an indoor condition, the effect of environmental conditions was at the lowest level. In other words, there was no change in wind speed or clouding of air. Finally, the starting and
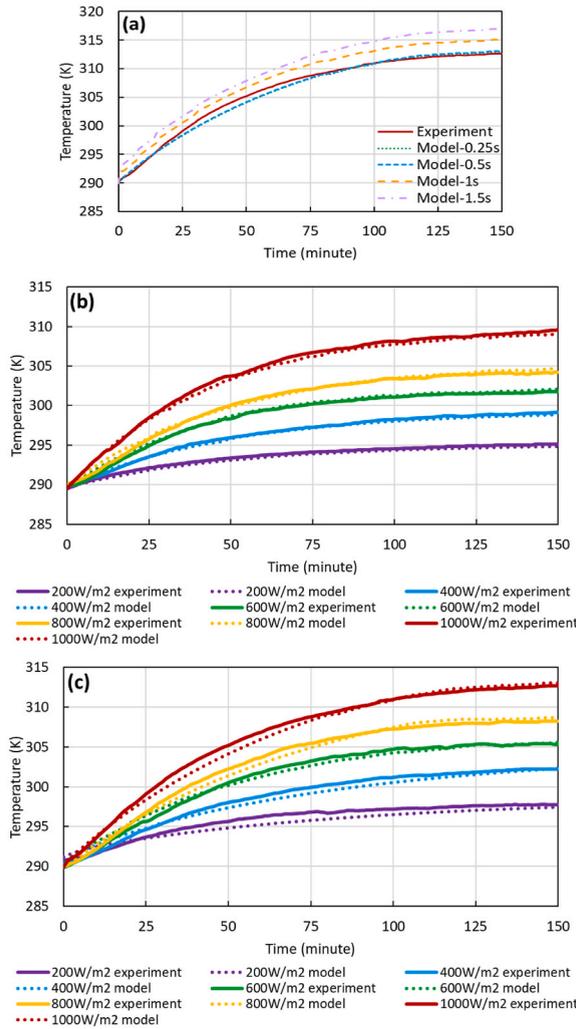
Fig. 10. (a) Comparison of time step sizes on temperature distribution, average temperature of (a) water, and (b) Al$_2$O$_3$/water nanofluid inside the cavity at four different irradiances.

finishing times of the experiment were kept the same for all the cases to maintain the same period cooling. Further as illustrated in Fig. 7, the standard deviation is under 1 for both fluids.

The extinction coefficients of Al$_2$O$_3$/water nanofluid and pure water are illustrated in Fig. 8(a). Water can be regarded as a translucent medium within the solar spectrum range of 0.2–1.2 μm, and it becomes an efficient absorber when the spectral irradiance shifts to the near-infrared band [44]. Since 85% of energy of the sunlight reaches the earth's crust in this solar spectrum range [45], adding nanoparticles to pure water can further increase absorption in these wavelength ranges (Fig. 8(a)). The behavior of water and nanofluid in the wavelength range is coherent with the work of Rabbi et al. [13] and Bhalla et al. [3]. Consequently, the impacts on the temperature distribution in the storage cavity under different heat fluxes are investigated using pure water (Fig. 8(b)) and Al$_2$O$_3$/water nanofluid (Fig. 8(c)). It is seen that both the heat transfer fluids have the same temperature rise trend. Increasing the radiation permeating the glass surface from 200 to 1000 W/m^2 means that the fluid in the storage cavity is exposed to a stronger and more intense light energy. This results in an augmentation in the heat transfer interaction between the heat transfer fluid and the radiation, thus improving the temperature gain. Further, due to the improved thermophysical and optical behaviours of nanofluid (Fig. 8(c)), the temperature rise is prominent compared to that of pure water (Fig. 8(b)). It is also observed that the temperature variation within the collector diminishes from the top (T_1) to the bottom (T_3) along the collector depth due to lessening of light power. It is also found that, however, this decline diminishes with the decrease of the heat flux. In addition, since both water and Al$_2$O$_3$/water nanofluids nearly reach a steady state from the 125th minutes, the temperature gain is approximately stable.

Fig. 9 presents the results of the impacts of the wind speed on water and Al$_2$O$_3$/water nanofluid. It is detected that the temperature rise diminishes when the wind velocity augments from 1 to 4 m/s in both fluids. The improvement in the wind speed induces the forced convective currents coming to the collector's glass layer to become more concentrated. This negatively impacts the temperature rise by enhancing the thermal losses from the collector to the atmosphere and decreasing the fluid's heat capture. As a result of the decrease in
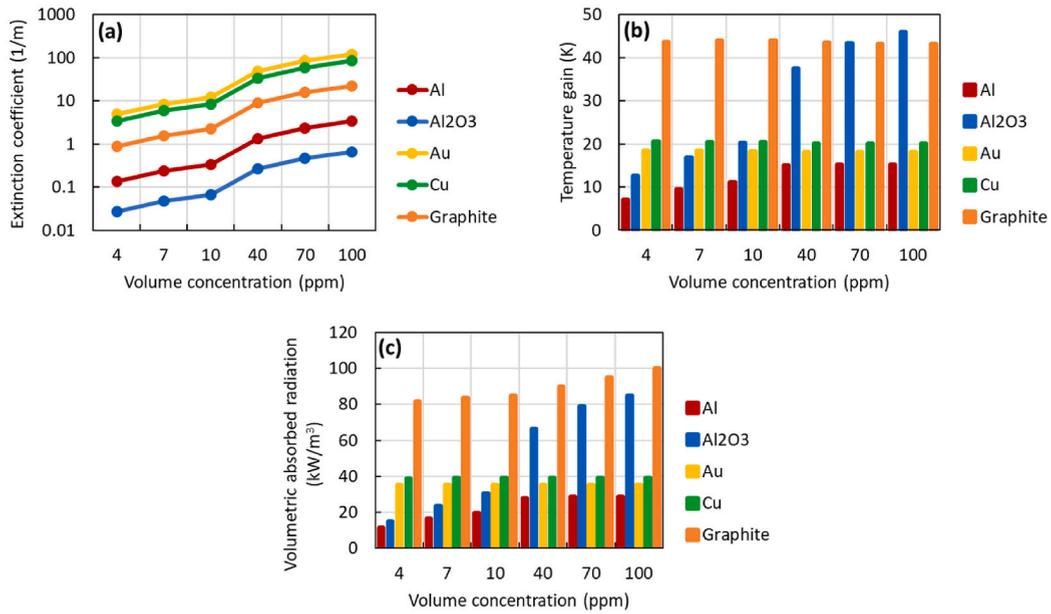
Fig. 11. Impact of different types of water-based mono nanoparticles: (a) extinction coefficient as logarithmic scale (m^{-1}), (b) temperature gain (K), and (c) volumetric absorbed radiation (kWm^{-3}) with various volume concentrations.

the wind speed, PCP enhances by improving the average temperature rise. It is also unearthed that the temperature rise at constant wind speed diminishes (from T_1 to T_3) as one moves towards the collector's base (Fig. 9). The reason for this can be characterized by the influence of declining the light density with increasing collector depth. Furthermore, it is monitored that the temperature variation is more homogeneous in the collector when the wind speed is 1 and 2 m/s. The decrease in the heat losses in parallel with the decreasing forced convective currents leads to this finding. This reduction in the collector performance, which diminishes as the speed enhances, is also encouraged by the research of Khanna et al. [46] and Farzan et al. [47].

Furthermore, the numerical model is validated with the experimental data set. The same optical, nanofluid and radiation heat transfer models described in Section 2 are used, but the simulation is run under the unsteady state condition to mimic the experiment. The different time step (*dt*) sizes as 0.25, 0.5, 1, and 1.5 s are applied to get closer and more uniform results compared to experiment. As demonstrated in Fig. 10(a), the final average temperatures are 312.9, 313, 315, and 317 K respectively, for the time step sizes of 0.25, 0.5, 1, and 1.5 s while the final experimental mean temperature is 312.7 K. Thus, *dt* is set to 0.5 s for better numerically stable results. Fig. 10(b and c) also demonstrates that there is a concordance between the experimental results and the numerical examination. The mean temperatures of both the water and the Al$_2$O$_3$/water nanofluid in the storage cavity increase during the applied radiation time, and both the fluids reach steady state after 125 min. The average temperature also enhances with increasing heat flux from 200 to 1000 W/m^2. Further, behaviour of the experimental average temperatures of the heat transfer fluids with respect to time are in line with those obtained by Guo et al. [17] and Zhang et al. [4].

4.2. Numerical investigation of thermal factors influencing the photothermal conversion performance

As illustrated in the previous part, there is a good concurrence between the experimental findings and numerical model. It means that the current numerical model can be expanded in order to deeply analyse and understand the PCP. The numerical outcomes also highlight the impacts of the particle size and volume concentration, nanoparticle type, tilt angle and base fluid type, which are the important factors in regard to the PCP in the storage system.

4.2.1. Effect of nanoparticle type and volume concentration on photothermal conversion

The effect of different types of mono nanoparticles as oxide (Al$_2$O$_3$), carbon based (Graphite) and metal (Al, Au, Cu) dispersed in water on the PCP is investigated under varying volume concentration in a solar collector, as indicated in Fig. 11(a). This figure signifies that the average extinction coefficient in the wavelength range as a function of volume concentration is also consistent with the studies of Kaluri et al. [33], Dugaria et al. [48], and Esmaeili et al. [49]. The increased attenuation improves the working fluid's heat capacity by augmenting the light-to-heat transition from the nanofluid by enabling the nanoparticles in the water, even at low volume concentrations (Fig. 11(c)). With the enhancing heat energy, the nanofluid's temperature rise increases up to a maximum of 45 K, as clarified in Fig. 11(b), and the improvement in the temperature gain is 7.33 times better than pure water. This is again found to be consistent with that of Beicker et al. [21] and Guo et al. [17] who explored the photothermal conversion augmentation using nanoparticles and increase in their volume concentrations.

Moreover, increasing the volume concentration not only enhances the working fluid's extinction coefficient, but also improves its thermal conductivity. Nanofluid with improved thermal conductivity causes collisions and displacements between each other due to
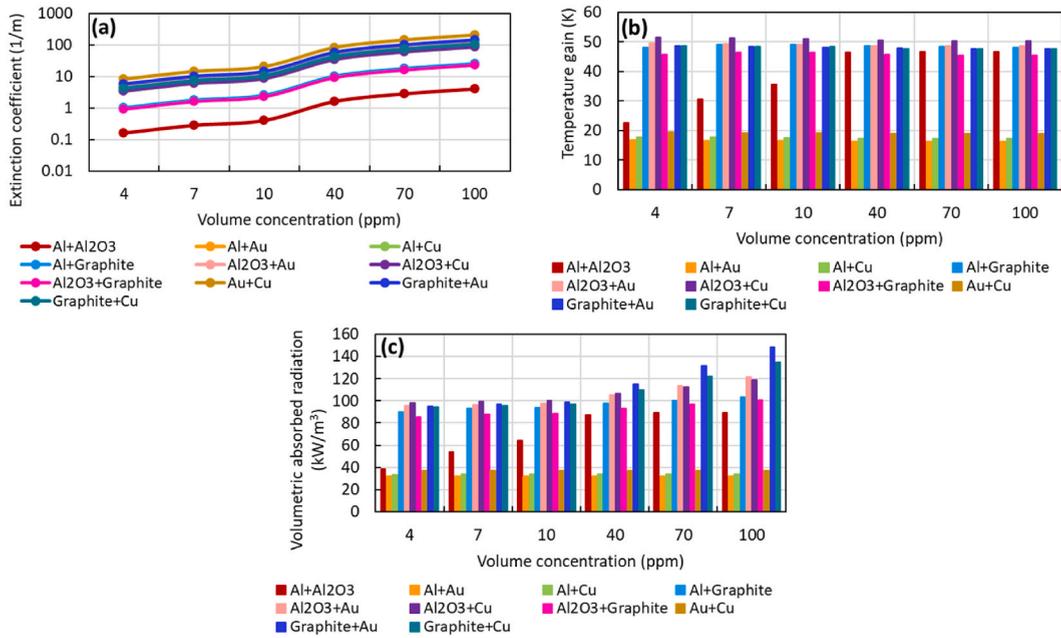
Fig. 12. Impact of different types of water-based blended nanoparticles: (a) extinction coefficient as logarithmic scale (m^{-1}), (b) temperature gain (K), and (c) volumetric absorbed radiation (kWm^{-3}) with various volume concentrations.

increase in nanoparticle molecules. It thus contributes to the temperature gain of Al/water and Al_2O_3/water nanofluids by performing more heat conversion at lower volume concentrations (4–40 ppm). Furthermore, increasing volume concentration makes the nanofluid more viscous, however, it limits the nanoparticles' movement in the host fluid, and the increase in other nanofluid types has been almost constant, as also demonstrated in Fig. 11(b).

In addition to the fluid viscosity, the enhancement in the volume concentration further leads to the nanofluid to absorb irradiation around the top wall, thereby increasing the heat conversion around the upper wall. In parallel with the enhanced heat conversion, it causes an increase in heat losses from the collector to the atmosphere. This may be a second possibility, which may create the temperature gain in the nanofluid to increase slowly or be stable. This also accords with our previous observation [35] which showed that the nanofluid's maximum temperature achieves the fixed state. Furthermore, since the Graphite's thermal conductivity, that is a type of carbon nanoparticle, is better than other particles, it ensures that the heat generation by the radiation is maximum (Fig. 11(c)), although its extinction coefficient is not maximum (Fig. 11(a)).

4.2.2. Effect of blended nanoparticles on photothermal conversion

The photothermal conversion of hybrid nanoparticles compared to mono nanoparticles is investigated in this section. Attenuation of hybrid nanoparticles is higher than mono nanoparticles (Fig. 12(a)) as it is equal to the total coefficient of mono nanoparticles forming the particle. Depending on the increasing attenuation, it enhances the solar thermal capture capacity of the hybrid nanofluid, which consists of hybrid nanoparticles that are uniformly dispersed by being added to water, allowing the hybrid nanoparticles to absorb more solar radiation. Therefore, increased absorbance augments the amount of heat that can be produced by the radiation in the nanofluid and subsequently contributes to the further heating of the nanofluid, and as also seen in Fig. 12(c), where the maximum temperature gain reaches up to 52 K. Thus, the amount of heat generation as a result of radiation in the collector reaches 150 kW/m^3 as in Fig. 12(c).

It was shown in Fig. 11(b and c) that the Al/water nanofluid has the lowest thermal capabilities while the performance of Al_2O_3/ water nanofluid improved with increasing volume concentration. Therefore, $Al + Al_2O_3$/water hybrid nanofluid is particularly formed to further investigate the thermal performance. It is clearly noticed in Fig. 12(b) that the newly formed hybrid nanofluid augments the temperature rise of the Al/water nanofluid as 214.3%, 215.8%, 215.3%, 209.5%, 206.7% and 206.5%, respectively, when the volume concentration boots from 4 to 100 ppm. Volumetric absorbed radiation is also found to enhance at the same volume concentrations by 245.5%, 237.5%, 236.8%, 222.2%, 210.9% and 210.1%, respectively (Fig. 12(c)). However, improvements in both the temperature gain and volumetric absorbed radiation are found to diminish with increasing volume concentration. The first cause for this is associated with the increasing particle concentration, causing the nanofluid becomes more viscous, as a result limiting its movement in the collector and consequently reducing the formation of convection currents. A second reason is that the enhanced volume concentration rises the thermal losses to the ambient by enhancing the nanoparticles' temperature gain at the vicinity of the collector's upper surface.
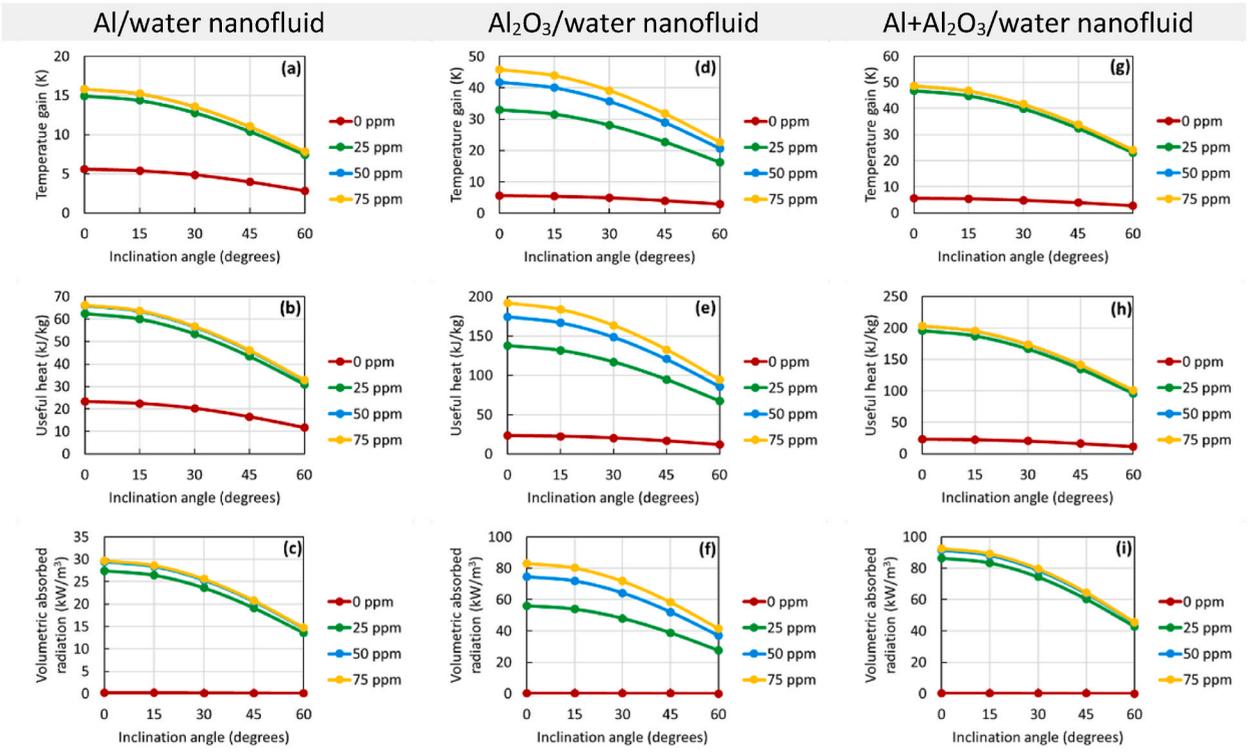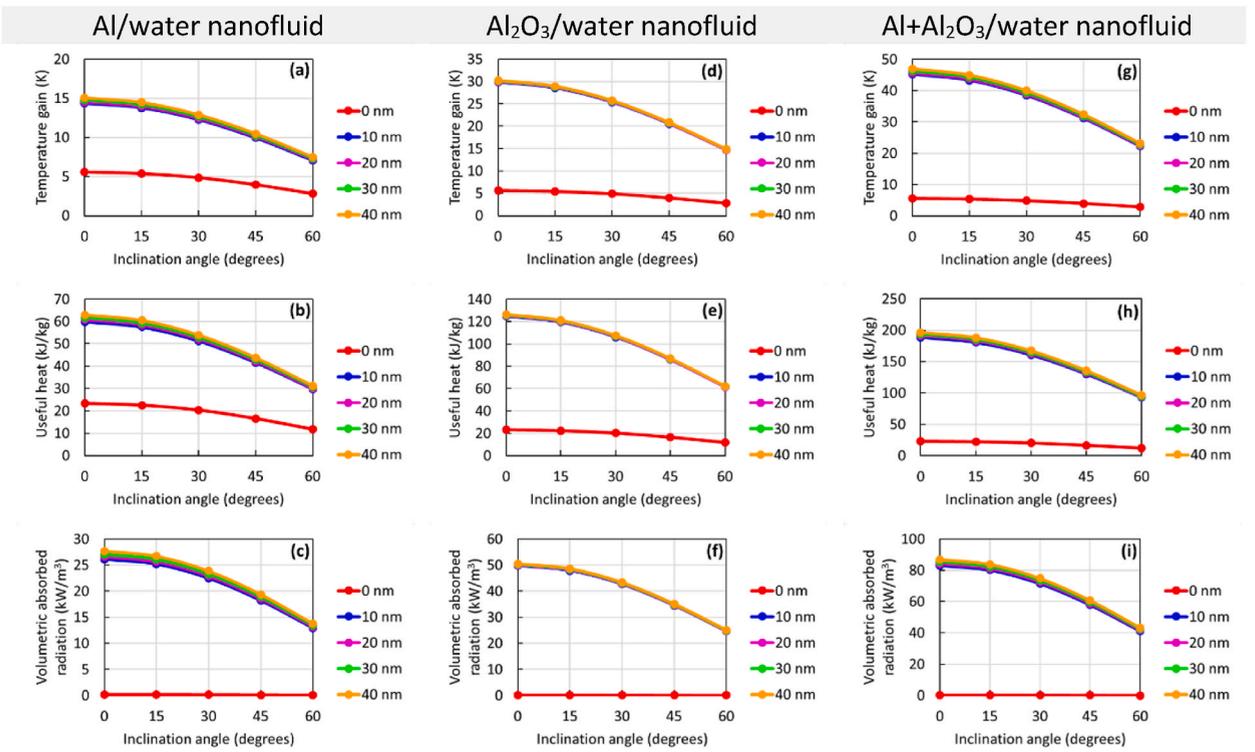
Fig. 13. Impact of inclination angle on the PCP (temperature gain (K), useful heat (kJkg^{-1}), and volumetric absorbed radiation (kWm^{-3})) for Al/water (a–c), Al$_2$O$_3$/water (d–f) and Al + Al$_2$O$_3$/water (g–i) nanofluids with various volume concentrations.
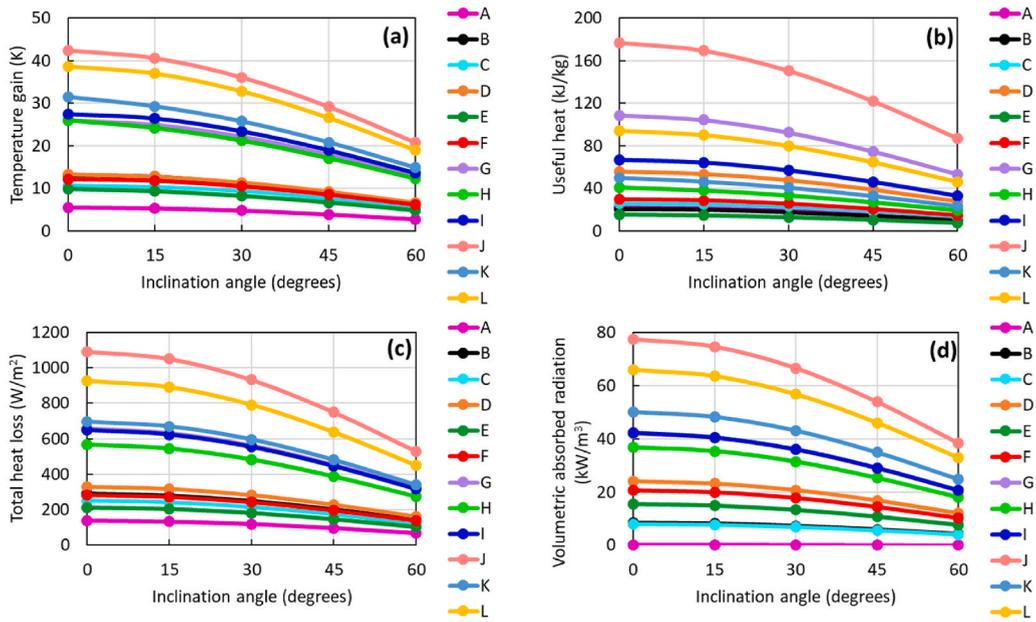
Fig. 14. Impact of inclination angle on the PCP (temperature gain (K), useful heat (kJkg^{-1}), and volumetric absorbed radiation (kWm^{-3})) for Al/water (a–c), Al$_2$O$_3$/water (d–f) and Al + Al$_2$O$_3$/water (g–i) nanofluids at volume concentration of 20 ppm with different nanoparticle sizes.

A: Water. **B**: Therminol VP1. **C**: Ethylene glycol. **D**: Water/Al. **E**: Therminol VP1/Al.
F: Ethylene glycol/Al. **G**: Water/Al$_2$O$_3$. **H**: Al2O3/Therminol VP1. **I**: Al2O3/Ethylene glycol.
J: Al+Al2O3/Water. **K**: Al+Al2O3/Therminol VP1. **L**: Al+Al2O3/Ethylene glycol.

Fig. 15. Impact of inclination angle on the PCP (a) temperature increment (K), (b) useful heat (kJkg^{-1}), (c) total heat loss (Wm^{-2}) and (d) volumetric radiation (kWm^{-3}) at particle concentration of 15 ppm with different base fluid types.

4.2.3. Effect of inclination angle on photothermal conversion

The impact of varying collector inclination angle on the PCP is investigated by using water-based Al, Al$_2$O$_3$ and Al + Al$_2$O$_3$ nanofluids. The reason for chosen these nanofluids is that, as reported in the previous sections, they demonstrated having better thermal performances. In Fig. 13, the effects of volume concentration and tilt angle, which are two different factors, on the thermal performance are shown. Enhancing the volume concentration from 0 ppm to 25 ppm at a fixed tilt angle augments the absorption ability of the sun rays penetrating the collector by the nanoparticles. The developed solar capacity in the nanofluid further boots the PCP, resulting an improvement in the temperature gain for all the three nanofluids studied (Fig. 13(a-d-g)). Useful heat gain of the collector also augments with increasing temperature gain (Fig. 13(b-e-h)). In addition, added nanoparticles absorb sunlight, further increasing the volumetric absorption capacity generated by radiation in the collector (Fig. 13(c-f-i)). For instance, when the absorption capacity of pure water is 0.145 kW/m^3 at an angle of inclination of 30°, the capacity of Al + Al$_2$O$_3$/water nanofluid increases to 75, 78 and 79.5 kw/m^3 respectively, as the volume concentration increases from 25 ppm to 50 ppm.

The second factor is that an increase in the tilt angle at a given volume concentration causes a diminish in the power of the working fluid to capture the sunbeam. Due to the decreasing photothermal conversion process, the nanofluid's temperature rise at a constant volume concentration diminishes with increasing tilt angle (Fig. 13(a-d-g)). Decreased temperature gain also negatively affects the useful heat gain of the collector (Fig. 13(b-e-h)). For instance, the useful heat gain of Al$_2$O$_3$/water nanofluid at a volume concentration of 75 ppm decreases from 192 to 94 kJ/kg with the improvement of the inclination angle from 0° to 60°. Finally, the volumetric absorption capacity of nanofluids by absorbing radiation also declines (Fig. 13(c-f-i)). Furthermore, decrease in the thermal performance can be further explained as follows. For instance, changing the angle of inclination negatively affects the combined radiation and free convection heat transfer. As a result, enhancing tilt angle diminishes the effects of natural convection by reducing the effect of buoyancy forces inside the collector. Due to this, it diminishes the heat that nanoparticles produce by radiation, subsequently adversely affecting its performance.

4.2.4. Effect of nanoparticle size on photothermal conversion

As displayed in Fig. 14(a-d-g), increasing the particle size slowly enhances the nanofluid's temperature rise. For example, when the size of the particles in the Al + Al$_2$O$_3$/water nanofluid increases from 0 nm to 40 nm at an inclination angle of 45°, the temperature gains are 3.96, 31.23, 31.53, 31.96 and 32.43 K, respectively. Accordingly, the useful heat gain of nanofluid, which is proportional to the temperature, augments (Fig. 14(b-e-h)). Likewise, the heat gains of Al + Al$_2$O$_3$/water nanofluids are 16.54, 130.47, 131.75, 133.54 and 135.49 kJ/kg, respectively. Improving the particle size also causes a development in the volumetric absorption generation by radiation in the nanofluid (Fig. 14(c-f-i)).

Besides, diminishing the collector inclination angle at a fixed particle size improves the nanofluids' thermal behaviour by enhancing the solar energy absorbance capacity. For example, temperature, useful heat gains and volumetric heat generation by
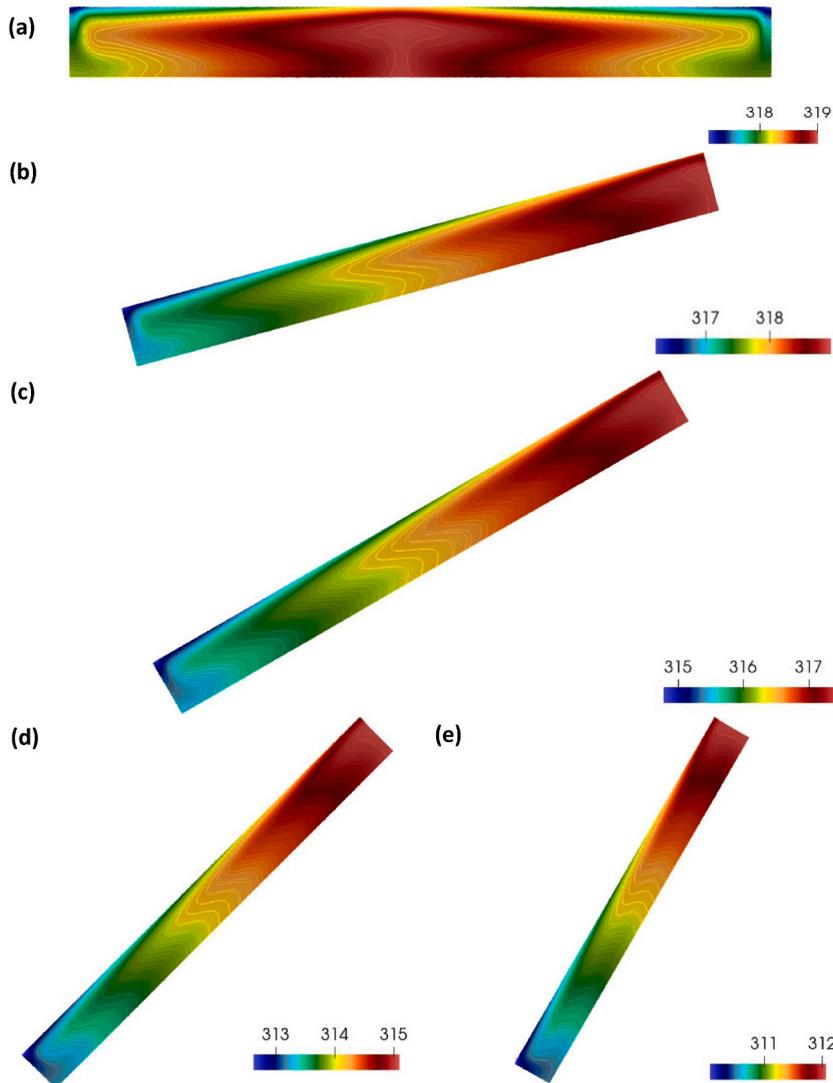
Fig. 16. Temperature (Kelvin, K) profiles of water/Al nanofluid at particle concentration of 20 ppm for different collector angles (a) 0°, (b) 15°, (c) 30°, (d) 45° and (e) 60°.

dispersion of nanoparticles with 40 nm size in Al/water nanofluids range from 7.46 to 15.07 K (Fig. 14(a)), 31.18–62.96 kJ/kg (Fig. 14 (b)), 13.77–27.69 kW/m^3 (Fig. 14(c)) respectively, with the decrease of the collector inclination from 60 to 0°. The performance improvement, which is inversely proportional to the collector inclination angle, agrees with the work of Hachicha et al. [50]. However, as the inclination angle diminishes, the buoyancy effect of the heat transfer fluid improves, and thus free convection develops further within the collector. The performance of the working fluid, whose heat transfer behaviour is increased, augments in the radiation-related heat production in the collector and thus further improves its performance.

4.2.5. Effect of base fluid on photothermal conversion

The thermal capacity of the solar collector is compared using Therminol VP1, ethylene glycol and water. Therminol VP1 has a higher temperature gain in pure heat transfer fluids without nanoparticle effect (Fig. 15(a)). Despite this high heat gain, ethylene glycol, which is the pure heat transfer fluid, has the highest useful heat gain due to the ethylene glycol's better specific heat behaviour (Fig. 15(b)). Further, due to the Therminol VP1's high temperature rise, it causes the collector's upper plate temperature to be higher, resulting in higher heat losses to the environment compared to other pure heat transfer fluids (Fig. 15(c)). The volumetric heat generation of Therminol VP1 is also slightly better than that of ethylene glycol, since the temperature gain is dependent on the volumetric heat generation (Fig. 15(d)).

Nanoparticle addition to the pure fluids enhances the fluid's thermophysical and optical behaviours. Due to these developing characteristics, the nanofluid captures more solar energy and boosts the volumetric heat generation. The water-based blended Al + Al$_2$O$_3$ nanofluid has the supreme volumetric heat generation (Fig. 15(d)) and the heat gain (Fig. 15(a)) becomes the highest for
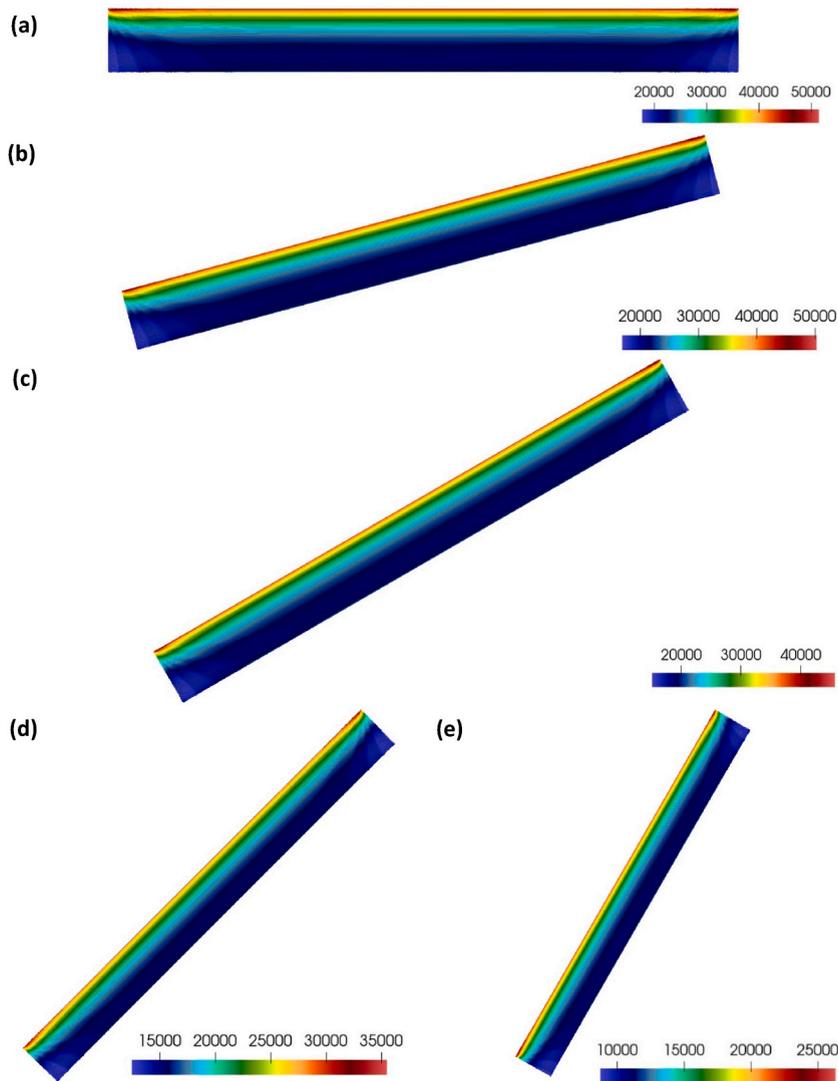
Fig. 17. Volumetric absorbed radiation (Wm^{-3}) profiles of water/Al nanofluid at particle concentration of 20 ppm for different collector angles (a) 0°, (b) 15°, (c) 30°, (d) 45°nd (e) 60°.

nanofluid. Thus, the Al + Al$_2$O$_3$/water hybrid nanofluid's useful heat gain is the highest compared to the other heat transfer fluids (Fig. 15(b)). Finally, due to the high temperature gain of the Al + Al$_2$O$_3$/water nanofluid, the collector's upper plate temperature is higher compared to the other fluids, thus more temperature loss occurs (Fig. 15(c)). For instance, when the slope angle is 0°, the collector's top wall temperature is 309.48 K and 344.69 K for pure water and Al + Al$_2$O$_3$/water nanofluid, respectively, while this temperature is 306.79 K and 324.29 K for 60°. In this case, increasing the collector inclination angle diminishes the working fluid's temperature rise, causing the top wall temperature to decline. One of the factors affecting this decrease in performance, which is independent of the type of base fluid, is the decrease of the buoyancy force with increasing inclination angle. Another factor is that the reduced buoyance force affects the heat transfer negatively, reducing the working fluid's heat generation from radiation. Hence, it diminishes the average thermal capacity of the fluid by declining the temperature rise.

4.2.6. Understanding the heat transfer and flow physics

In order to deeply understand the process of flow and heat transfer physics of the heat transfer fluid, temperature and volumetric absorbed radiation contours are analysed in this part. The influence of various collector angles on the temperature and volumetric absorbed radiation distributions is first presented in Figs. 16 and 17 respectively. As seen, an increase in the inclination angle from 0° (Fig. 16(a)) to 60° (Fig. 16(e)) causes the nanofluid to not absorb radiation at a sufficient level due to the decrease in the sunbeam's penetration into the collector. Therefore, the nanofluid's maximum temperature in the collector drops from 319 K (Fig. 16(a)) to 312 K (Fig. 16(d)), and the useful heat that the collector can store declines. Depending on the decreasing temperature inside the collector, the collector's upper plate temperature diminishes and heat transfer to the ambient lessens.
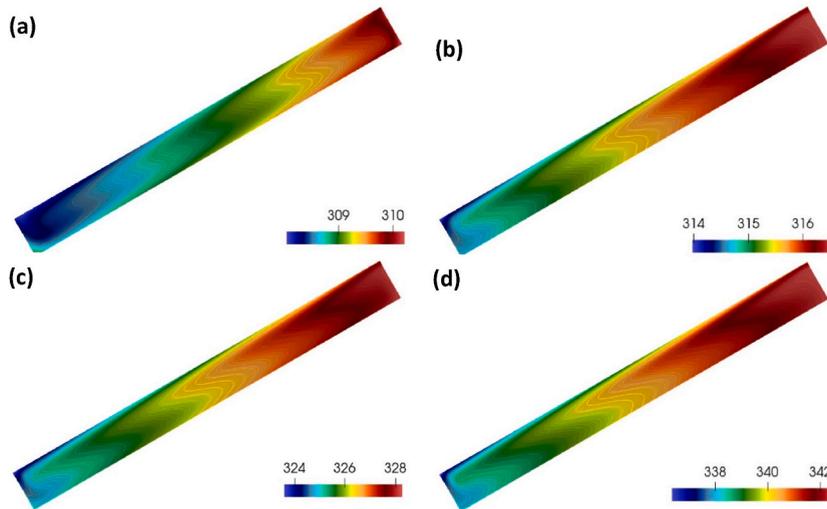
Fig. 18. Temperature (Kelvin, K) profiles at inclination angle of 30° for (a) pure water, (b) Al/water, (c) Al$_2$O$_3$/water and (d) Al + Al$_2$O$_3$/water nanofluids at volume concentration of 15 ppm.
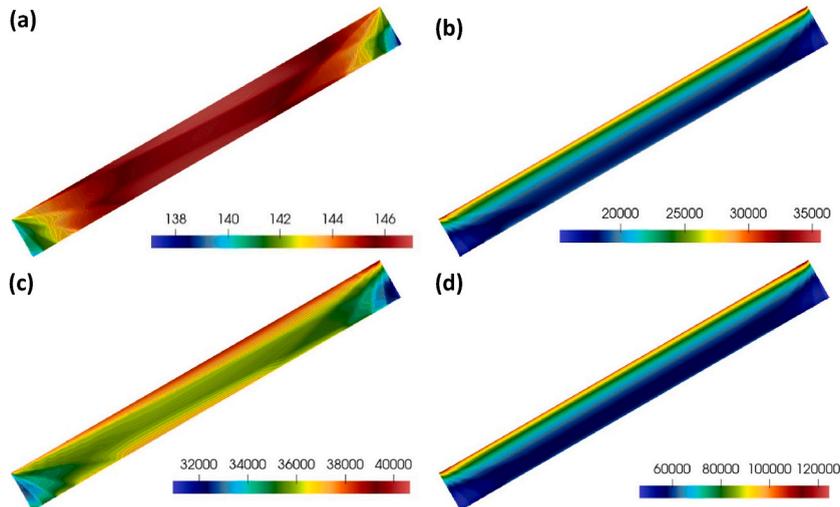

Fig. 19. Volumetric absorbed radiation (Wm^{-3}) profiles at inclination angle of 30° for (a) pure water, (b) Al/water, (c) Al$_2$O$_3$/water and (d) Al$_2$O$_3$+Al/water nanofluids at volume concentration of 15 ppm.

Furthermore, due to the highly reflective properties of the side and bottom walls, sunbeam is reflected towards the inner part of the collector by striking these walls. Due to the impact of the buoyancy force, as seen in Fig. 16(a), the heated nanofluid moves upwards from the collector's core. Due to the merged radiation and convection thermal losses from the collector's top part to the environment, the top layer encounters the cold nanofluid around it, and this cold nanofluid causes the collector to move downwards from the periphery of the upper edge. As the collector angle increases, however, the thermal boundary layers develop along the length, allowing the hot and cold zones to form in the solar collector's upper and base zones, respectively, with the impact of the buoyant force. The fluid core may be stagnant because of natural convection, the influence of buoyancy, and the angle of tilt.

Moreover, an enhancement in the collector angle means a decrease in the irradiation intensity affecting the nanoparticles dispersed in the water. Decreased radiation energy negatively impacts the PCP of the collector by causing a diminish in the volumetric absorbed radiation of the nanofluid in the collector as described in Fig. 17. Further, nanoparticles augment the scattering of light by intensifying their reactions with radiation due to their capability to capture solar energy. Increasing scattering also reduces light intensity with increasing collector depth (Fig. 17). Last but not least, the utilization of nanoparticles ensures that more of the solar rays in the collector are caught around the collector's upper plate, allowing the top nanofluid layer to store more solar energy (Fig. 17).

The impact of various heat transfer fluids, which is the second factor, on the temperature distribution in the collector with an inclination angle of 30° is shown in Fig. 18, Fig. 19 while demonstrates the heat generation from the absorbed irradiation in the solar collector of these fluids. In the deficiency of nanoparticle impact (Fig. 18(a)), because the heat generation is at the lowest level due to
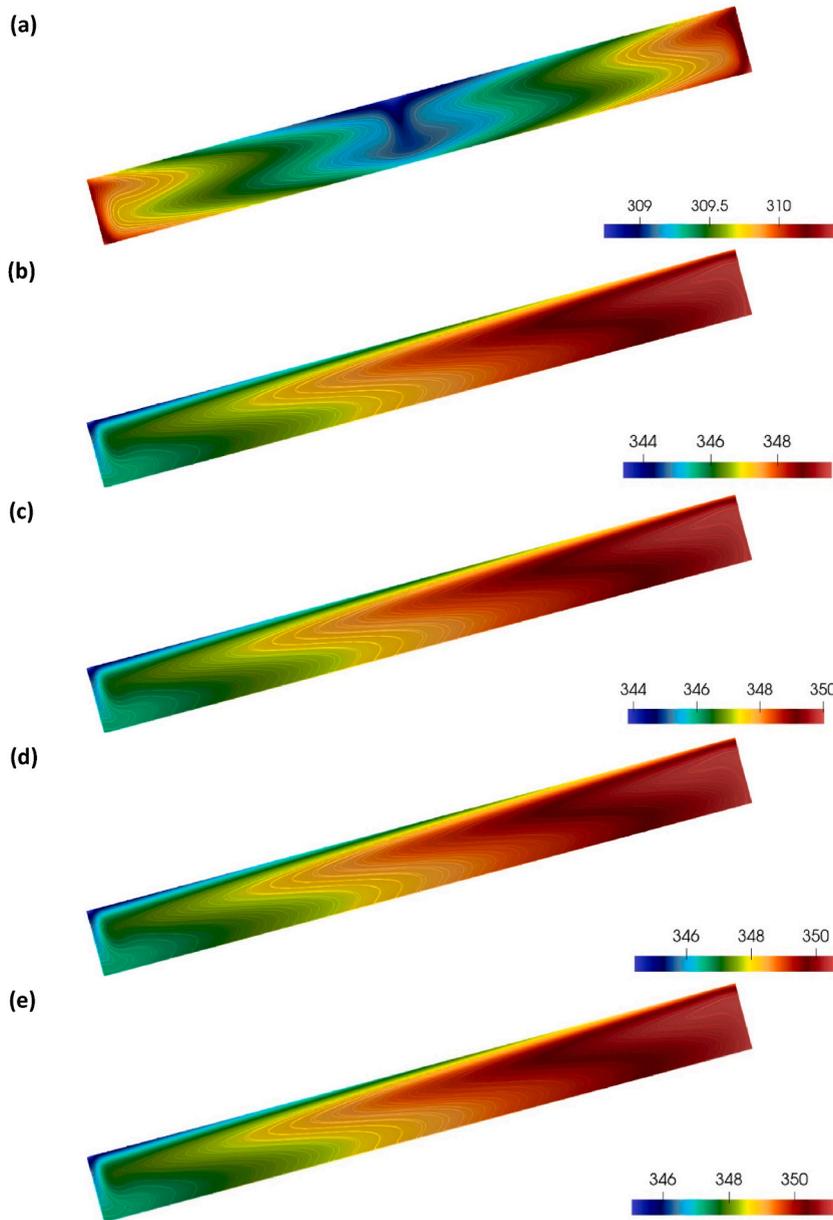
Fig. 20. Temperature (Kelvin, K) profiles of water/Al + Al$_2$O$_3$ nanofluid at particle concentration of 20 ppm and inclination angle of 15° for different particle sizes (a) 0 nm, (b) 10 nm, (c) 20 nm (d) 30 nm, and (e) 40 nm.

the low radiative properties of pure water (Fig. 19(a)), the pure water's temperature rise is the lowest as illustrated in Fig. 18(a). Al/water and Al$_2$O$_3$/water nanofluids, which are formed by dispersing Al and Al$_2$O$_3$ nanoparticles separately in pure water with a volume concentration of 15 ppm, increase the capacity of absorbing solar energy penetrating the collector. The increased absorption capacity significantly improves the heat generation in the collector in Al/water (Fig. 19(b)) and Al$_2$O$_3$/water (Fig. 19(c)) nanofluids compared to pure water. Thus, the temperature rise of both Al/water (Fig. 18(b)) and Al$_2$O$_3$/water (Fig. 18(c)) nanofluids occurs more than pure water. Hybrid nanofluids can also be used to further increase this temperature gain. For this, hybrid nanofluids can be prepared by uniformly dispersing Al + Al$_2$O$_3$ hybrid nanoparticles in pure water with the same volume concentration. As described in Fig. 19(d), the heat generation of this nanofluid is maximized due to its high attenuation and improved thermal conductivity so that as indicated in Fig. 18(a), the Al + Al$_2$O$_3$/water hybrid nanofluid has the highest temperature gain.

Furthermore, Figs. 20 and 21 display the impacts of nanoparticle diameter on temperature and absorbed radiation, respectively. The nanoparticle size being 0 nm indicates that the pure fluid does not contain nanoparticles. Thus, the radiation affecting the pure water has the lowest temperature gain, as in Fig. 20(a), due to the low absorption ability of water molecules. This is because, as indicated in Fig. 21(a), heat generation in pure water by not enough radiation is not possible. By adding nanoparticles with low
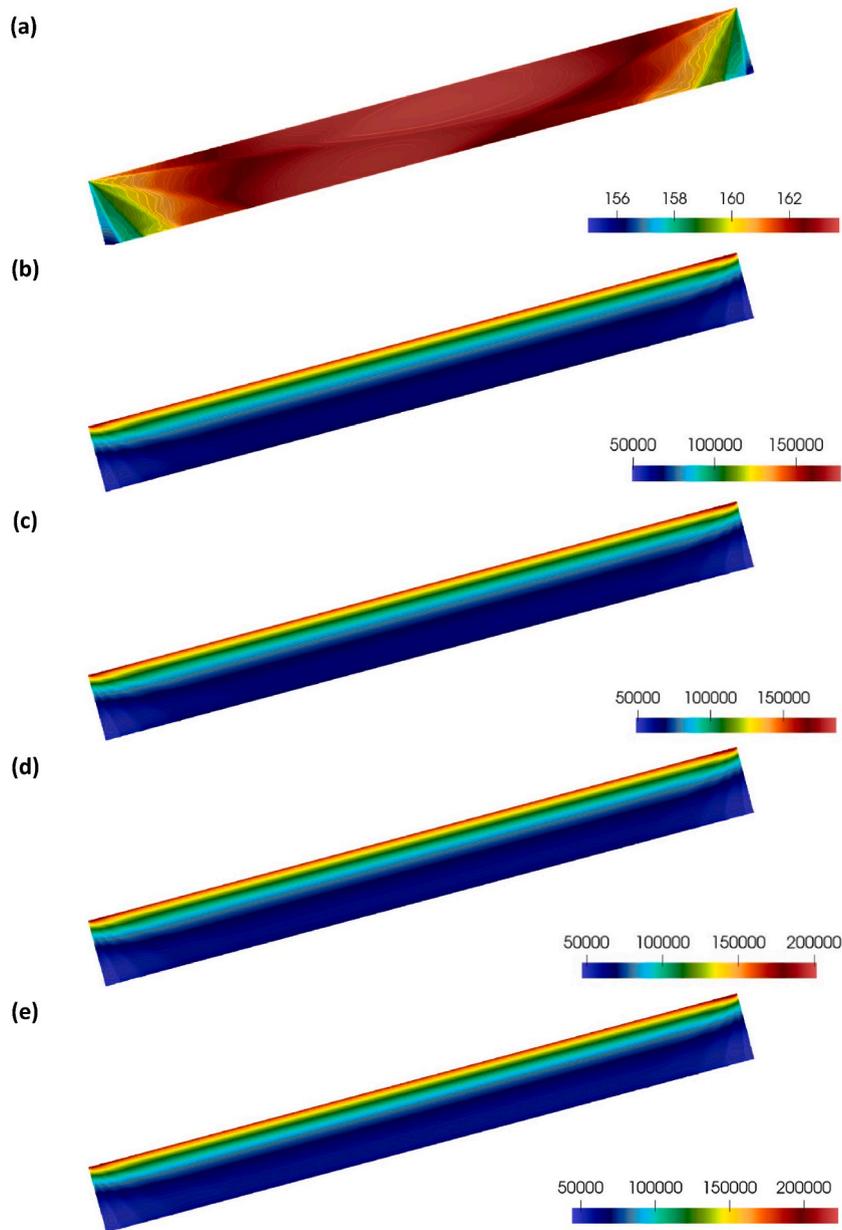
(a)

(b)

(c)

(d)

(e)

Fig. 21. Volumetric absorbed radiation (Wm^{-3}) profiles of Al + Al$_2$O$_3$/water nanofluid at particle concentration of 20 ppm and inclination angle of 15° for different particle sizes (a) 0 nm, (b) 10 nm, (c) 20 nm (d) 30 nm, and (e) 40 nm.

diameter (10 nm) to pure water, the working fluid's radiation absorption capacity is enhanced. Hence, by improving the PCP in the collector (Fig. 21(b)), both the temperature gain (Fig. 20(b)) and useful heat are improved. Furthermore, the enhanced particle size improves both the nanofluid's thermophysical and optical characteristics, enabling the nanofluid to absorb more radiation, further accelerating the radiation heat transfer, further developing the thermal heat conversion of the sun rays, and augmenting the collector performance (Figs. 20 and 21(c-e)).

In addition, as seen in Fig. 20(a), improving the nanoparticle diameter causes the nanofluid to heat more from the area near the base right of the collector due to the collector tilt angle and buoyancy force, and the hot fluid transports towards the inside of the collector in the horizontal direction, causing the colder fluid to flow into the collector. Moreover, the nanoparticle addition ensures that the heat conversion of the radiation occurs more in the upper region of the collector (Fig. 21(b–e)), allowing the pure water to be more uniformly distributed in the heat collector generated by the radiation (Fig. 21(a)). Finally, due to the insufficient absorption capacity of pure water, the cooling effect in the collector is more prominently than the nanoparticle effect (Fig. 20(a)).

Finally, the impacts of different base fluids on the temperature and volumetric absorbed radiation contours are represented in Figs. 22 and 23, respectively. Due to the water-based Al + Al$_2$O$_3$ hybrid nanofluid's ability to absorb irradiation more, it increases the
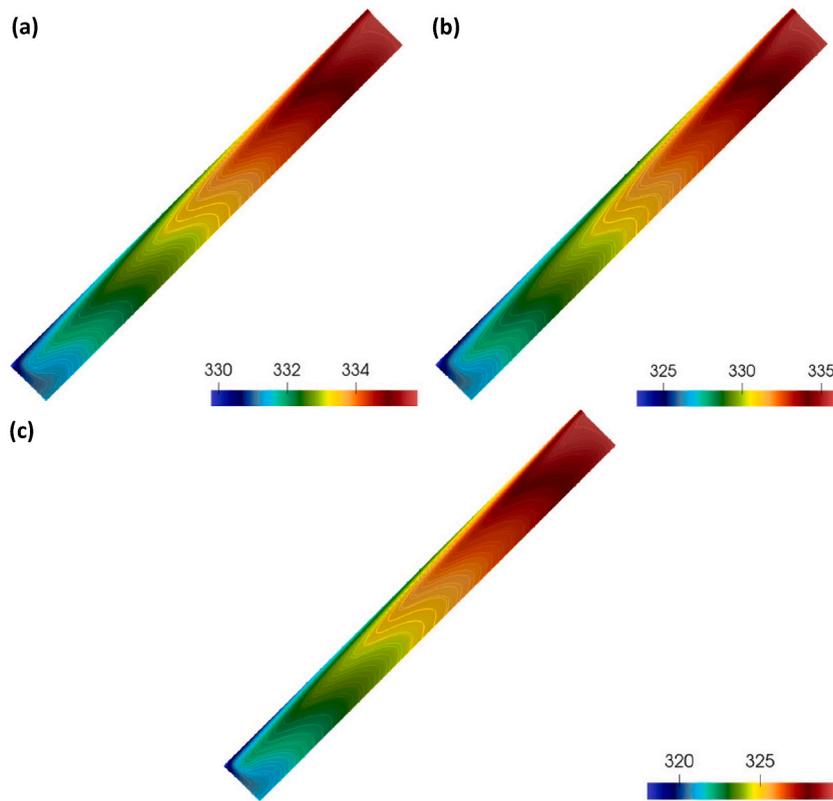
Fig. 22. Temperature (Kelvin, K) profiles at inclination angle of 45° for (a) Al + Al$_2$O$_3$/water, (b) Al + Al$_2$O$_3$/Ethylene glycol, and (c) Al + Al$_2$O$_3$/Therminol VP1 nanofluids at volume concentration of 15 ppm.

heat transmission between the nanoparticles and the water molecules more, allowing the temperature gain to occur more than the other base fluid types (Fig. 22(a)), and the heat generation in the collector is more than Ethylene glycol (Fig. 23(b)) and Therminol VP1 (Fig. 23(c)), ensuring the maximum useful heat gain as in Fig. 15(b). In addition, it is seen that the temperature distribution of the water-based hybrid nanofluid in the collector is more uniform (Fig. 22(a)).

5. Conclusions

The PCPs of various types of nanofluids in an inclined solar collector were investigated in this work. The impacts of particle size, collector inclination angle, volume concentration, nanoparticle type, and base fluid type on the PCP were examined. Analysis of two-dimensional fluid flow and combined radiation and free convection heat transfer using the DO method that included absorption, emitting and scattering effects were performed using ANSYS Fluent 2020 R1. The experimental system was set up for numerical validation, and the numerical results matched well with the experimental data.

The findings revealed that the utilization of nanoparticles augmented the capability of the heat transfer fluid to capture and absorb solar energy. The nanofluid's temperature increment improved due to the enhancement in the heat generation in the collector by radiation, thus the useful heat was improved. With the hybrid nanoparticles' addition to the host fluid, the nanofluid's PCP was further augmented at low volume concentrations. For instance, the useful heat gain at a volume concentration of 4 ppm of Al$_2$O$_3$/water nanofluid was increased by 3.9, 4.1, and 3.6 times when Au, Cu and Graphite nanoparticles were added, while volumetric absorbed radiation improved by 6.4, 6.6, and 5.7 times, respectively. In addition, increasing the collector inclination angle decreased the nanofluid's solar radiation absorption capacity, reducing the nanofluid's thermal capacity. The decreased thermal capabilities negatively affected the PCP. For instance, the temperature gains of the Al + Al$_2$O$_3$/water nanofluid were 48.7, 46.7, 41.6, 33.8, and 24.1 K, with an increase of 15° from the collector inclination angle from 0° to 60°, respectively.

In addition, enhancing the nanoparticle concentration at the constant tilt angle improved the thermal performance. As the water/Al + Al$_2$O$_3$ nanofluid's volume concentration boosted from 25 to 75 ppm, the volumetric absorbed radiation developed from 83.5 to 89.1 kw/m^3. Further, because the increase in nanoparticle size developed the nanofluid's optical behaviours, the enhancement in the particle diameter allowed the PCP to be enhanced by enhancing the temperature gain of the nanofluid at the constant collector tilt angle. Besides, when different types of pure base fluids were compared, the temperature gain in Therminol VP1 was better. Thus, the solar collector's upper plate temperature filled with pure Therminol VP1 soared, resulted in high thermal losses to the atmosphere. Furthermore, increasing the collector tilt angle ensured that the thermal boundary layers were formed along the length of the cavity. While the heated fluid by the impact of buoyancy force was collected in the upper region, the downward movement from the edges of
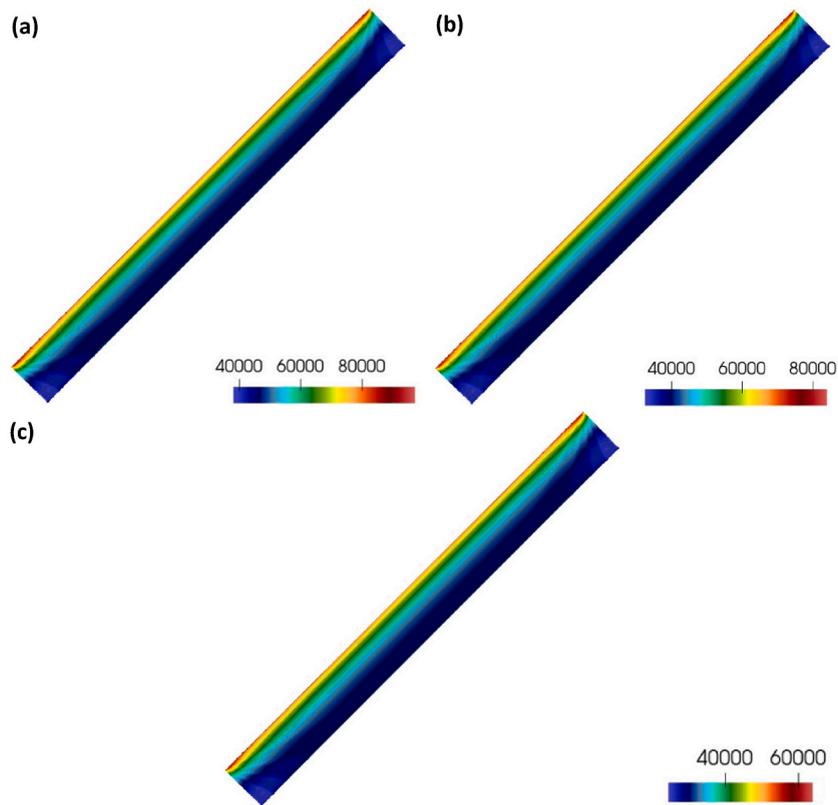
Fig. 23. Volumetric absorbed radiation (Wm^{-3}) profiles at inclination angle of 45° for (a) Al + Al$_2$O$_3$/water, (b) Al + Al$_2$O$_3$/Ethylene glycol, and (c) Al + Al$_2$O$_3$/Therminol VP1 nanofluids at volume concentration of 15 ppm.

the cold fluid collected in the lower region of the cold fluid. Moreover, the improvement in the nanoparticle concentration in the fixed collector angle augmented the attenuation of the nanofluid and enhanced the absorption of solar irradiation, however it caused a decrease in the collision of nanoparticles in the nanofluids with increased viscosity due to the Brownian motion. Lastly, the experimental study indicated that the utilization of nanofluids and the augmented of solar irradiation improved the temperature gain of the system. The experimental work also revealed that the PCP diminished with the wind velocity.

Consequently, this study showed that blended nanofluids can be simultaneously utilized as a working fluid and as a storage medium in a volumetrically/directly heated inclined solar collector. But, the collector tilt angle can be employed as a performance increasing/decreasing control parameter in solar energy systems.

Author statements

Oguzhan Kazaz: Conceptualisation, Methodology, Software, Validation, Investigation, Formal Analysis, Visualisation, Writing - original draft, Writing - review and editing. **Rosalia Ferraro**: Analysis, Writing - review and editing. **Manlio Tassieri**: Analysis, Writing - review and editing. **Shanmugam Kumar**: Supervision, Writing - review and editing. **Gioia Falcone**: Supervision, Writing - review and editing. **Nader Karimi**: Conceptualisation, Supervision, Writing - review and editing. **Manosh C. Paul**: Conceptualisation, Methodology, Supervision, Writing - review and editing, Project administration, Resources, Funding acquisition.

Declaration of competing interest

The authors declare that they have no known competing financial interests or personal relationships that could have appeared to influence the work reported in this paper.

Data availability

All data supporting this study are provided in full in the Results and discussion section of the paper and will also be available from the corresponding author upon reasonable request.

Acknowledgments

References

[1] A. Ahmadi, M.A. Ehyaei, A. Doustgani, M. El Haj Assad, A. Hmida, D.H. Jamali, R. Kumar, Z.X. Li, A. Razmjoo, Recent residential applications of low-temperature solar collector, J. Clean. Prod. 279 (2021), 123549.

[2] M.R. Saffarian, M. Moravej, M.H. Doranehgard, Heat transfer enhancement in a flat plate solar collector with different flow path shapes using nanofluid, Renew. Energy 146 (2020) 2316–2329.

[3] V. Bhalla, H. Tyagi, Parameters influencing the performance of nanoparticles-laden fluid-based solar thermal collectors: a review on optical properties, Renew. Sustain. Energy Rev. 84 (2018) 12–42.

[4] H. Zhang, H.-J. Chen, X. Du, G. Lin, D. Wen, Dependence of photothermal conversion characteristics on different nanoparticle dispersions, J. Nanosci. Nanotechnol. 15 (4) (2015) 3055–3060.

[5] A.Z. Sahin, M.A. Uddin, B.S. Yilbas, A. Al-Sharafi, Performance enhancement of solar energy systems using nanofluids: an updated review, Renew. Energy 145 (2020) 1126–1148.

[6] S. Suman, M.K. Khan, M. Pathak, Performance enhancement of solar collectors—a review, Renew. Sustain. Energy Rev. 49 (2015) 192–210.

[7] O. Kazaz, N. Karimi, S. Kumar, G. Falcone, M.C. Paul, Numerical investigation of the influences of nanoparticle size and tilt angle in a directly absorption solar system, in: 14th International Conference on Applied Energy (ICAE2022), 2022. Bochum, Germany.

[8] R. Yang, X. Li, F. Yin, J. Shi, D. Jing, The mechanism of enhanced photothermal conversion of low-dimensional plasmonic nanofluids with LFPs resonance, Int. J. Heat Mass Tran. 208 (2023), 124056.

[9] O. Kazaz, N. Karimi, S. Kumar, G. Falcone, M.C. Paul, Effects of combined radiation and forced convection on a directly capturing solar energy system, Therm. Sci. Eng. Prog. 40 (2023), 101797.

[10] O. Kazaz, N. Karimi, S. Kumar, G. Falcone, M.C. Paul, Effects of nanofluid's base fluid on a volumetric solar collector, in: 11th International Conference on Renewable Power Generation - Meeting Net Zero Carbon, (RPG 2022), Hybrid Conference, London, UK, 2022.

[11] X. Li, H. Wang, H. Zhang, L. Yang, Comprehensive performance evaluation of Ti3C2 MXene/TiN composite nanofluids for photo thermal conversion, Appl. Therm. Eng. 228 (2023), 120486.

[12] P. Raj, S. Subudhi, A review of studies using nanofluids in flat-plate and direct absorption solar collectors, Renew. Sustain. Energy Rev. 84 (2018) 54–74.

[13] H.M.F. Rabbi, A.Z. Sahin, B.S. Yilbas, A. Al-Sharafi, Methods for the determination of nanofluid optical properties: a review, Int. J. Thermophys. 42 (9) (2021) 1–42.

[14] O. Kazaz, N. Karimi, G. Falcone, S. Kumar, M.C. Paul, Effect of radiative heat transfer in nanofluid for volumetric solar collector, in: 13th International Conference on Applied Energy (ICAE2021), 2021. Thailand/Virtual.

[15] J. Lin, W. Li, S. Zhao, H. Liu, C. Xu, X. Ju, Experimental investigation on the optical properties of ag nanofluids under high temperatures, Int. Commun. Heat Mass Tran. 135 (2022), 106059.

[16] E. Sani, N. Papi, L. Mercatelli, G. Żyła, Graphite/diamond ethylene glycol-nanofluids for solar energy applications, Renew. Energy 126 (2018) 692–698.

[17] H. Guo, W. Liu, Q. Shu, H. Zhu, J. Yang, L. Xiao, Full-spectrum photo-thermal conversion of plasmonic LaB6 nanofluids, Mater. Lett. 308 (B) (2022), 131261.

[18] P.G. Kumar, S. Vigneswaran, M. Meikandan, D. Sakthivadivel, M. Salman, A.K. Thakur, R. Sathyamurthy, S.C. Kim, Exploring the photo-thermal conversion behavior and extinction coefficient of activated carbon nanofluids for direct absorption solar collector applications, Environ. Sci. Pollut. Control Ser. 29 (2022) 13188–13200.

[19] L. Huaxu, W. Fuqiang, L. Dong, Z. Jie, T. Jianyu, Optical properties and transmittances of ZnO-containing nanofluids in spectral splitting photovoltaic/thermal systems, Int. J. Heat Mass Tran. 128 (2019) 668–678.

[20] M. Hatami, D. Jing, Evaluation of wavy direct absorption solar collector (DASC) performance using different nanofluids, J. Mol. Liq. 229 (2017) 203–211.

[21] C.L. Beicker, M. Amjad, E.P. Bandarra Filho, D. Wen, Experimental study of photothermal conversion using gold/water and MWCNT/water nanofluids, Sol. Energy Mater. Sol. Cell. 188 (2018) 51–65.

[22] M. Turkyilmazoglu, Performance of direct absorption solar collector with nanofluid mixture, Energy Convers. Manag. 114 (2016) 1–10.

[23] M. Hatami, S. Mosayebidorcheh, D. Jing, Thermal performance evaluation of alumina-water nanofluid in an inclined direct absorption solar collector (IDASC) using numerical method, J. Mol. Liq. 231 (2017) 632–639.

[24] V. Cregan, T.G. Myers, Modelling the efficiency of a nanofluid direct absorption solar collector, Int. J. Heat Mass Tran. 90 (2015) 505–514.

[25] ANSYS Fluent User's Guide, ANSYS, Inc., Canonsburg, 2013.

[26] H. Tyagi, P. Phelan, R. Prasher, Predicted efficiency of a low-temperature nanofluid-based direct absorption solar collector, J. Sol. Energy Eng. 131 (4) (2009), 041004-041007.

[27] C.F. Bohren, D.R. Huffman, Absorption and Scattering of Light by Small Particles, Wiley, New York, 1983.

[28] G.M. Hale, M.R. Querry, Optical constants of water in the 200-nm to 200-μm wavelength region, Appl. Opt. 12 (3) (1973) 555–563.

[29] E.D. Palik, Handbook of Optical Constants of Solids, Academic Press, 1997.

[30] M. Bass, C.M. DeCusatis, J.M. Enoch, V. Lakshminarayanan, G. Li, C. MacDonald, V.N. Mahajan, E.V. Stryland, Handbook of optics, in: Optical Properties of Materials, third ed. vol. IV, Nonlinear Optics, Quantum Optics, 2009.

[31] L.G. Schulz, The optical constants of silver, gold, copper, and aluminum. I. The absorption coefficient k, J. Opt. Soc. Am. 44 (5) (1954) 357–362.

[32] L.G. Schulz, F.R. Tangherlini, Optical constants of silver, gold, copper, and aluminum. II. The index of refraction n, J. Opt. Soc. Am. 44 (5) (1954) 362–368.

[33] R. Kaluri, S. Vijayaraghavan, S. Ganapathisubbu, Model development and performance studies of a concentrating direct absorption solar collector, J. Sol. Energy Eng. 137 (2) (2015), 021005.

[34] J.A. Duffie, W.A. Beckman, Solar Engineering of Thermal Processes, John Wiley & Sons, Inc., New Jersey, 2013. Hoboken.

[35] O. Kazaz, N. Karimi, S. Kumar, G. Falcone, M.C. Paul, Enhanced sensible heat storage capacity of nanofluids by improving the photothermal conversion performance with direct radiative absorption of solar energy, J. Mol. Liq. 372 (2023), 121182.

[36] P. Ternik, Conduction and convection heat transfer characteristics of water–Au nanofluid in a cubic enclosure with differentially heated side walls, Int. J. Heat Mass Tran. 80 (2015) 368–375.

[37] K. Khanafer, K. Vafai, M. Lightstone, Buoyancy-driven heat transfer enhancement in a two-dimensional enclosure utilizing nanofluids, Int. J. Heat Mass Tran. 46 (19) (2003) 3639–3653.

[38] B. Ghasemi, S.M. Aminossadati, Periodic natural convection in a nanofluid-filled enclosure with oscillating heat flux, Int. J. Therm. Sci. 49 (1) (2010) 1–9.

[39] O.Z. Sharaf, A.N. Al-Khateeb, D.C. Kyritsis, E. Abu-Nada, Direct absorption solar collector (DASC) modeling and simulation using a novel Eulerian-Lagrangian hybrid approach: optical, thermal, and hydrodynamic interactions, Appl. Energy 231 (2018) 1132–1145.

[40] Y. Cengel, M. Boles, Thermodynamics, An Engineering Approach, 2015.

[41] M.F. Modest, Radiative Heat Transfer, Academic Press, 2013.

[42] S. Kumar, A. Kumar, N. Chander, D.K. Singh, Thermal performance analysis of a novel direct absorption solar collector augmented solar still using silver nanofluids, Environ. Prog. Sustain. Energy 41 (5) (2022), e13858.

[43] B.V. Balakin, M. Stava, A. Kosinska, Photothermal convection of a magnetic nanofluid in a direct absorption solar collector, Sol. Energy 239 (2022) 33–39.

[44] M. Du, G.H. Tang, Plasmonic nanofluids based on gold nanorods/nanoellipsoids/nanosheets for solar energy harvesting, Sol. Energy 137 (2016) 393–400.

[45] C.V. Vital, S. Farooq, R.E. de Araujo, D. Rativa, L.A. Gómez-Malagón, Numerical assessment of transition metal nitrides nanofluids for improved performance of direct absorption solar collectors, Appl. Therm. Eng. 190 (2021), 116799.

[46] S. Khanna, K.S. Reddy, T.K. Mallick, Optimization of solar photovoltaic system integrated with phase change material, Sol. Energy 163 (2018) 591–599.

[47] H. Farzan, E.H. Zaim, M. Ameri, T. Amiri, Study on effects of wind velocity on thermal efficiency and heat dynamics of pavement solar collectors: an experimental and numerical study, Renew. Energy 163 (2021) 1718–1728.

[48] S. Dugaria, M. Bortolato, D.D. Col, Modelling of a direct absorption solar receiver using carbon based nanofluids under concentrated solar radiation, Renew. Energy 128 (2018) 495–508. Part B.

[49] M. Esmaeili, M. Karami, S. Delfani, Performance enhancement of a direct absorption solar collector using copper oxide porous foam and nanofluid, Int. J. Energy Res. 44 (7) (2020) 5527–5544.

[50] A.A. Hachicha, I. Al-Sawafta, Z. Said, Impact of dust on the performance of solar photovoltaic (PV) systems under United Arab Emirates weather conditions, Renew. Energy 141 (2019) 287–297.